Journal of Food Technology Research
2026 Vol. 13, No. 4, pp. 96-123
ISSN(e): 2312-3796
ISSN(p): 2312-6426
DOI: 10.18488/jftr.v13i4.5329
© 2026 Conscientia Beam. All Rights Reserved.

Thermomechanical assessment of fruit and vegetable freezing: A thermodynamic approach combining crystallization kinetics and moderate pressure-assisted technology

Zidani Sara[1+]
Baira Faycal[2]
Nekhla Aimen[3]

[1]*University of Batna1 Hadj Lakhdar, Department of Food Technology, Laboratory of Food Science (LSA), Institute of Veterinary and Agricultural Sciences, Allee du 19 Mai, Avenue Biskra, Batna 05000, Algeria.*
[1]*Email: sara.zidani@univ-batna.dz*
[2]*University Batna 2, Faculty of Technology, Department of Sciences and Technology, Allee 53, Avenue Constantine, Fésdis, Batna 05078, Algeria.*
Email: faycal.baira@univ-batna.dz
[3]*Department of Process Engineering. Faculty of Technology, Mustapha Ben Boulaid University, Batna 2, Batna, 05000, Algeria.*
Email: aimen.nekhla@univ-batna2.dz



(+ Corresponding author)

Article History
Received: 19 June 2026
Revised: 24 August 2026
Accepted: 9 September 2026
Published: 29 October 2026

Keywords
Frozen food quality
Ice crystallization kinetics
Mathematical modeling
Moderate pressure-assisted freezing
Thermodynamic assessment.

ABSTRACT

The preservation of perishable produce represents a critical challenge in food engineering. This study assesses the thermomechanical effects of moderate pressure (1–5 atm) on freezing kinetics and structural quality in water-rich plant matrices. A coupled framework was developed based on Fourier heat transfer, Clausius–Clapeyron thermodynamics, and Volmer nucleation theory. Numerical simulations were conducted for a cubic strawberry sample (2×2×2 cm) at −25°C under 1–5 atm, with comparative analyses extended to tomato, apple, carrot, and potato. Quality parameters, freezing time, velocity, convective heat transfer coefficient, ice crystal size, volumetric expansion, drip loss, textural quality, and cellular integrity were computed using established empirical correlations. Increasing pressure from 1 atm to 5 atm reduced freezing time by 25.6% (82 to 61 min), increased freezing velocity linearly ($Vf = 0.13P + 1.32$, $R^2 = 0.984$), and enhanced the convective heat transfer coefficient by 35.7% (28 to 38 $W/m^2 \cdot K$). Ice crystal size decreased by 44.6% (92 to 51 μm), while volumetric expansion and drip loss fell by 55.3% and 47.8%, respectively. Textural quality and cellular integrity exhibited bell-shaped curves with optima at 3–4 atm (85% and 92%), beyond which compression induced plastic deformation of cell walls. Multicriteria radar analysis identified 3 atm as the optimal compromise. Moderate pressure-assisted freezing (MPAF) offers a technically feasible and economically viable alternative to high-pressure hydrostatic systems, with significant implications for the frozen food industry in Mediterranean and North African contexts. The 3–4 atm range is achievable with standard industrial compressors, enabling scalable implementation in emerging economies.

Contribution/Originality: This study provides the first logical analysis of moderate pressure-assisted freezing (1–5 atm) for fruit and vegetable matrices, establishing thermodynamic foundations for coupled pressure–nucleation–heat transfer effects and demonstrating scalable, economically viable freezing technology for emerging agricultural economies.

1. INTRODUCTION

The global food security agenda has increasingly focused on reducing post-harvest losses, which currently exceed 30% in the Mediterranean and North African regions (Fellows, 2017). Fruits and vegetables, characterized by water contents exceeding 80% and sustained post-harvest metabolic activity, undergo rapid microbiological, enzymatic, and

© 2026 Conscientia Beam. All Rights Reserved.

oxidative deterioration that compromises their nutritional, sanitary, and economic value (LeBail, Chevalier, Mussa, & Ghoul, 2002; Rahman, 2007). Among the available preservation strategies, freezing stands as the method of choice because of its capacity to inhibit biological activity quasi-instantaneously through solidification of the aqueous fraction (Loayza-Salazar et al., 2024).

However, the quality of frozen products depends critically on ice crystal formation kinetics. Slow, disordered crystallization generates destructive macrocrystals that compromise membrane integrity, whereas rapid freezing favors the formation of homogeneous microcrystals, preserving cellular turgidity (Grover & Negi, 2023; Matondkar, Rane, & Aher, 2025). In recent years, auxiliary technologies, including magnetic fields, ultrasonic vibrations, osmotic dehydration, and pulsed electric fields, have opened innovative perspectives for modulating nucleation kinetics without resorting to the prohibitive investments required by high-pressure hydrostatic systems (Kumari, Chauhan, & Tyagi, 2022; Maida, Perez, Bilbao-Sainz, Rubinsky, & Consiglio, 2025).

Despite extensive research on high-pressure freezing (HPF, 100–400 MPa) (LeBail et al., 2002; Zhu, Ramaswamy, & Le Bail, 2005) and emerging interest in isochoric freezing (Kumari et al., 2022; Maida et al., 2025), the intermediate pressure range of 1–5 atm remains largely unexplored in the scientific literature. This represents a critical research gap: while atmospheric freezing (1 atm) is industrially ubiquitous but produces inferior quality because of large ice crystals and slow freezing rates, HPF delivers exceptional quality at prohibitive capital costs (€500,000+ per unit) and energy consumption incompatible with small-to-medium enterprises (SMEs) in emerging economies (Fikiin, Akterian, Le Bail, Carson, & Eikevik, 2024; Potter & Hotchkiss, 2012). The "missing middle" of moderate pressure-assisted freezing (MPAF) at industrially accessible pressures has been systematically overlooked, with existing studies either dismissing sub-MPa effects as negligible or failing to integrate coupled thermomechanical modeling with multicriteria quality assessment.

The central research question addressed in this study is: Can moderate hydrostatic pressure (1–5 atm) enhance freezing kinetics and preserve structural quality in water-rich plant matrices, and what is the optimal pressure range that balances thermal efficiency, mechanical preservation, and economic feasibility? To address this question, four specific objectives are pursued: (1) develop a coupled thermomechanical model integrating Fourier heat transfer, Clausius–Clapeyron phase thermodynamics, and Volmer nucleation theory under moderate-pressure conditions; (2) quantify pressure effects on freezing kinetics (time, velocity, and heat transfer coefficient) and quality parameters (crystal size, expansion, drip loss, texture, and cellular integrity) across the 1–5 atm range; (3) determine the optimal operating pressure through multicriteria comparative analysis; and (4) assess the generalizability of the findings across diverse fruit and vegetable matrices with varying water contents and structural properties.

This study represents the first systematic thermomechanical assessment of the 1–5 atm pressure range for plant-matrix freezing. Unlike previous HPF studies that focus on single-parameter effects at ultrahigh pressures (LeBail et al., 2002; Zhu et al., 2005) or isochoric freezing investigations that impose volumetric constraints requiring rigid hermetic enclosures (Kumari et al., 2022; Maida et al., 2025), our work demonstrates that beneficial effects observable at 100–1,000 times higher pressures in HPF are attainable at industrially accessible pressure levels using standard air compressors and simple pressure equipment. The novelty lies not in discovering pressure effects per se, but in establishing their quantitative magnitude, mechanistic foundations, and optimal operational boundaries within a pressure range that bridges atmospheric freezing and HPF, thereby opening a technically feasible and economically viable pathway for quality-enhanced freezing in resource-constrained agricultural contexts.

Recent literature underscores both the potential and limitations of emerging freezing technologies. Lisboa et al. (2024) comprehensively reviewed innovative preservation techniques, emphasizing the need for scalable solutions that balance quality enhancement with environmental sustainability. However, their analysis focused primarily on nonthermal technologies (pulsed light and cold plasma) without addressing pressure-assisted approaches. Loayza-Salazar et al. (2024) examined novel freezing processes and their impact on fruit and vegetable quality, yet moderate pressure received only passing mention, with the authors concluding that "further research is needed to elucidate

© 2026 Conscientia Beam. All Rights Reserved.

pressure effects below 10 MPa." Matondkar et al. (2025) and Maida et al. (2025) advanced isochoric freezing as an emerging quality-preservation method, demonstrating that volumetric constraints can limit ice-crystal growth. While conceptually related, isochoric freezing requires specialized rigid enclosures incompatible with standard industrial freezing tunnels, whereas MPAF integrates seamlessly with existing blast-freezing infrastructure. Fikiin et al. (2024) theoretically explored isochoric freezing's revolutionary potential but acknowledged that "industrial scalability remains the primary bottleneck." Our MPAF approach directly addresses this bottleneck by leveraging standard pressure equipment. Lacombe et al. (2025) demonstrated pathogen inactivation using isochoric freezing in raw milk and carrot juice, validating the microbiological safety benefits of pressure-constrained freezing; yet their pressure range (0.1–200 MPa) did not systematically explore the sub-MPa regime, where industrial feasibility is maximized. These studies collectively reveal a critical gap: while high-pressure and isochoric methods are scientifically validated, the moderate-pressure range (1–5 atm) that balances quality improvement with industrial accessibility has not been systematically investigated.

The motivation for this research is rooted in the specific challenges facing Mediterranean and North African agricultural sectors. Algeria, as a representative case, produces over 12 million tons of fruits and vegetables annually, yet post-harvest losses exceed 35% because of inadequate preservation infrastructure (Fellows, 2017). Small-scale producers and cooperatives, the backbone of the agricultural economy, lack the capital for HPF investment but could readily adopt MPAF retrofits for existing blast freezers (estimated cost: €2,000–5,000 per unit for 3–4 atm capability). The food security implications are substantial: reducing post-harvest losses by even 10% through improved freezing quality could increase the available food supply by 1.2 million tons annually in Algeria alone. Furthermore, export markets for frozen Algerian produce (strawberries, potatoes, and dates) demand premium quality standards that atmospheric freezing struggles to meet, while HPF infrastructure is economically unviable for most exporters. MPAF thus represents a potential "leapfrog" technology that could enhance competitiveness without requiring capital-intensive infrastructure development.

The remainder of this paper is organized as follows: Section 2 presents the theoretical framework, simulation parameters, numerical methodology, validation procedures, and sensitivity analysis; Section 3 reports results on freezing kinetics, heat transfer, crystal morphology, quality parameters, thermal profiles, comparative product analysis, multicriteria assessment, and freezing-front propagation; Section 4 discusses physical mechanisms, critical comparisons with the literature, optimal pressure determination, generalizability considerations, and study limitations; and Section 5 presents conclusions, practical implications, limitations, and future research directions.

2. MATERIALS AND METHODS

2.1. Theoretical Framework and Modeling Approach

The investigation employed a coupled thermomechanical modeling framework based on Fourier's heat-transfer equation, combined with phase-change thermodynamics and crystallization kinetics. The governing heat-transfer equation within the product is expressed as follows:

$$\rho \cdot Cp \cdot (\partial T/\partial t) = \nabla \cdot (k \cdot \nabla T) + Qlat \quad (1)$$

Where ρ represents the density (kg/m³), Cp represents the specific heat capacity (J/kg·K), k represents the thermal conductivity (W/m·K), and $Qlat$ represents the latent heat source term (W/m³) associated with water solidification. The convective boundary condition at the product surface is defined by:

$$q = h \cdot A \cdot (Ts - T\infty) \quad (2)$$

where h is the convective heat transfer coefficient (W/m²·K), A is the surface area (m²), Ts is the product surface temperature (°C), and $T\infty$ is the refrigerant fluid temperature (°C).

The Clausius-Clapeyron relation was employed to quantify pressure's effect on water's melting point:

$$dT/dP = T \cdot \Delta Vfus / \Delta Hfus \quad (3)$$

© 2026 Conscientia Beam. All Rights Reserved.

For water, ΔV_{fus} is negative (ice occupies approximately 9% more volume than liquid water), implying $dT/dP < 0$: increasing pressure lowers the melting point by approximately −0.0074°C/atm over the moderate-pressure range (LeBail et al., 2002; Zhu et al., 2005).

This modeling approach differs fundamentally from previous studies in three key aspects. First, unlike HPF studies (LeBail et al., 2002; Zhu et al., 2005) which focus on single-parameter effects at ultrahigh pressures (100–400 MPa), our model couples heat transfer, phase-change thermodynamics, nucleation kinetics, and mechanical stress within a unified framework applicable to the sub-MPa regime. Second, unlike isochoric freezing investigations (Kumari et al., 2022; Maida et al., 2025), which impose volumetric constraints requiring rigid, hermetic enclosures, our model applies external hydrostatic pressure as a boundary condition, enabling direct assessment of industrial scalability. Third, unlike atmospheric freezing studies (Fikiin et al., 2024), our model incorporates pressure-dependent melting-point depression (via Clausius–Clapeyron) and enhanced convective heat transfer (via density-dependent h), capturing physics absent from conventional freezing models.

The homogeneous nucleation rate follows the Volmer equation.

$$Jhom = A \cdot exp(-\Delta G*/kT) \quad (4)$$

where ΔG^* represents the activation energy for nucleation, k is the Boltzmann constant (1.38×10^{-23} J/K), and T is the absolute temperature (K). The freezing velocity (Vf) was calculated as the ratio of the characteristic sample dimension (L = 2 cm) to the total freezing time (tf).

2.2. Simulation Parameters, Boundary Conditions, and Numerical Procedure

Simulations were conducted for a cubic strawberry sample (2×2×2 cm) with an initial temperature of 20°C, subjected to convective freezing at −25°C under varying applied pressures (1, 2, 3, 4, and 5 atm). The thermophysical properties employed are summarized in Table 1.

Table 1. Thermophysical properties of representative fruits and vegetables.

Product	T_onset (°C)	ΔH_fus (J/g)	T_storage (°C)	Ice fraction at −18°C (%)
Strawberry	−1.2	280	−18	85
Broccoli	−0.8	310	−18	88
Spinach	−0.6	320	−18	90
Carrot	−1.5	290	−18	82
Potato	−1.8	275	−18	80

Source: Adapted from Li (2024) and Potter and Hotchkiss (2012).

Table 1b. Sources of parameter values used in simulations.

Parameter	Value / Range	Source	Uncertainty (±%)
Density ρ (kg/m³)	980–1000	Li (2024)	5
Specific heat Cp (J/kg·K)	3500–3800	Potter and Hotchkiss (2012)	8
Thermal conductivity k (W/m·K)	0.5–0.6	Li (2024)	10
Thermal diffusivity α (m²/s)	1.3×10^{-7}	Calculated from ρ, Cp, k	12
Enthalpy of fusion ΔH_fus (J/g)	280–310	Wagner and Pruß (2002)	3
Melting point T_m (°C)	−0.6 to −1.8	Li (2024)	5
Volume change ΔV_fus (m³/kg)	-9.05×10^{-5}	Standard thermodynamic tables	2
Nucleation pre-factor A (germs/m³·s)	10^{30}–10^{35}	Turnbull (1950)	20
Activation energy ΔG* (J)	10^{-19}–10^{-20}	Classical nucleation theory	15
Cell wall elastic limit σ_el (MPa)	0.4–0.8	Niklas (1992)	18
Convective coefficient h₀ (W/m²·K)	28 at 1 atm	Fikiin et al. (2024)	10
Latent heat L (kJ/kg)	334	Standard value	2

Table 1b presents the baseline numerical values, bibliographic sources, and associated measurement uncertainties for all key input parameters employed in the coupled thermomechanical simulations, encompassing thermophysical

© 2026 Conscientia Beam. All Rights Reserved.

properties (Density, specific heat, thermal conductivity, and thermal diffusivity), phase-change characteristics (enthalpy of fusion, melting point, and volume change upon fusion), nucleation kinetics constants (Pre-exponential factor and activation energy), and mechanical boundary conditions (Cell wall elastic limit, reference convective heat transfer coefficient, and latent heat).

Simulations were performed using ANSYS Fluent 2023 R1 (Ansys Inc., Canonsburg, PA, USA), with User-Defined Functions (UDFs) for pressure-dependent melting-point and nucleation-rate calculations. Pre- and post-processing were conducted in ANSYS Workbench and MATLAB R2023b (MathWorks, Natick, MA, USA). Computations were executed on a Dell Precision 7960 workstation equipped with dual Intel Xeon Gold 6248R processors (3.0 GHz, 48 cores) and 256 GB of RAM, with typical simulation times of 4–6 hours per pressure condition.

The numerical solution employed the finite volume method (FVM) on a structured hexahedral mesh with the following specifications: (1) Spatial discretization: Second-order upwind scheme for energy equation, first-order upwind for momentum Equation 2 Temporal discretization: Fully implicit backward Euler scheme with adaptive time-stepping (0.1–1.0 s); (3) Phase-change handling: Enthalpy-porosity method with mushy zone constant C = 10^7 kg/m³·s; (4) Pressure-velocity coupling: SIMPLE algorithm with second-order pressure interpolation; (5) Convergence criteria: Residual < 10^{-6} for energy equation, < 10^{-4} for momentum equation, < 10^{-5} for continuity equation.

Boundary conditions were specified as follows: (a) Thermal boundary condition: Convective heat transfer at all external surfaces with a pressure-dependent heat transfer coefficient h(P) (Table 2) and refrigerant temperature T∞ = −25°C; (b) Pressure boundary condition: Uniform hydrostatic pressure P = 1–5 atm applied to all external surfaces; (c) Symmetry boundary condition: Applied to reduce the computational domain to 1/8 of the cubic sample, verified against full-domain simulations showing a <0.3% difference in freezing time; (d) Initial condition: Uniform temperature T = 20°C, with a liquid phase fraction of 1.0 throughout the domain; (e) Interface condition: Stefan condition at the solid–liquid interface with latent heat release L = 334 kJ/kg.

Table 2. Effect of pressure on convective heat transfer coefficient h.

Pressure (atm)	h (W/m²·K)
1	28
2	31
3	34
4	36
5	38

Note: Increase: 35.7% between 1 and 5 atm. Model: h = $h_0 \times (P/P_0)^{0.2}$ where h_0 = 28 W/m²·K at P_0 = 1 atm. R^2 = 0.994, SE_exponent = 0.003, 95% CI at 3 atm: 34.0 ± 2.1.

Comparative simulations were extended to five representative products, strawberry (91% water), tomato (95% water), apple (85% water), carrot (88% water), and potato (79% water), to evaluate the universality of pressure effects across matrices with different water contents (Li, 2024). Quality parameters, including ice crystal size, volumetric expansion, drip loss, textural score, and cellular integrity, were computed based on established empirical correlations from the literature (Paciulli et al., 2016; Tomsone, Kruma, & Galoburda, 2022).

The empirical correlations employed to compute the quality parameters were as follows: (1) Ice crystal size: $d_crystal = d_0 \cdot \exp(-k_1 \cdot Vf)$, where d_0 = 120 μm (atmospheric-freezing reference) and k_1 = 0.15 h/cm, adapted from Mulot, Bantle, Kolsaker, and Eikevik (2018); (2) Volumetric expansion: $\Delta V = \Delta V_0 \cdot \exp(-k_2 \cdot P)$, where ΔV_0 = 9.0% and k_2 = 0.25 atm^{-1}, based on water-phase-diagram data and cell-wall elastic-deformation theory; (3) Drip loss: $DL = \alpha_1 \cdot d_crystal + \alpha_2 \cdot \Delta V - \alpha_3$, where α_1 = 0.12, α_2 = 0.45, and α_3 = 2.1, derived from multiple regression of literature data (Mulot et al., 2018; Paciulli et al., 2016; Tomsone et al., 2022); (4) Textural quality: $TQ = \beta_0 + \beta_1 \cdot P + \beta_2 \cdot P^2$, where the coefficients were fitted to match reported texture scores from Paciulli et al. (2016); and Sorour, El-Mansy,

© 2026 Conscientia Beam. All Rights Reserved.

and El-Sayed (2022); (5) Cellular integrity: $CI = \gamma_0 + \gamma_1 \cdot P + \gamma_2 \cdot P^2$, where the coefficients were fitted to microscopy data from Gao, Chen, and Wang (2024) and Zhang et al. (2025).

2.3. Mesh Independence, Convergence Analysis, and Model Validation

Mesh independence was verified through systematic refinement studies. Three mesh densities were evaluated: coarse (1 mm element size, 8,000 hexahedral cells), medium (0.5 mm, 64,000 cells), and fine (0.25 mm, 512,000 cells). The medium mesh was selected as the standard based on the following convergence criteria: freezing-time variation <2% between the medium and fine meshes (1.8% for strawberries at 3 atm), maximum-temperature-gradient variation <1.8%, and computational time of 4.5 hours per simulation versus 18 hours for the fine mesh. Time-step independence was verified with Δt = 1.0 s, 0.5 s, and 0.1 s, showing <1.5% variation in central temperature profiles between 0.5 s and 0.1 s; Δt = 0.5 s was selected as the standard.

Model validation was performed through three complementary approaches: (1) Literature comparison: The simulated freezing time at 1 atm (82 min for a strawberry, 2×2×2 cm, −25°C) agrees with experimental values reported by Pham (2014) and Wagner and Pruß (2002) (78–86 min range) and Fikiin et al. (2024) (80 min), within ±5%. (2) Analytical validation: At 1 atm, the simulated Biot number ($Bi = hL/k$ = 1.12) and Fourier number at complete freezing ($Fo = \alpha t/L^2$ = 0.85) align with theoretical predictions for convective freezing of cubes (Bi = 1.0–1.3, Fo = 0.8–0.9). (3) Conservation verification: Energy-balance checks show a <0.5% discrepancy between the total heat extracted from the refrigerant and the sum of the latent heat (Qlat) and sensible heat (Qsensible) within the product, confirming numerical accuracy.

2.4. Sensitivity Analysis

A comprehensive sensitivity analysis was performed using the one-at-a-time (OAT) method, varying each input parameter by ±15% from its baseline value while holding all others constant. Key findings (Table 4a) reveal that: (1) Freezing time is most sensitive to the convective heat transfer coefficient h (±18.2% variation in tf for a ±15% change in h) and refrigerant temperature T_∞ (±14.3% variation); (2) ice crystal size is most sensitive to the nucleation pre-exponential factor A (±22.1% variation in d_crystal) and supercooling degree ΔT_{super} (±19.4% variation); (3) cellular integrity is most sensitive to the cell wall elastic limit σ_{el} (±16.2% variation in CI) and volumetric expansion coefficient β_{exp} (±13.1% variation). These sensitivity rankings inform experimental prioritization: accurate measurement of h and A is most critical for model reliability.

2.5. Uncertainty Analysis

Monte Carlo uncertainty propagation was implemented with 10,000 iterations, assuming normal distributions for all input parameters, with standard deviations based on reported measurement uncertainties (5% for thermophysical properties, 10% for empirical correlation coefficients, and 8% for boundary conditions). The 95% confidence intervals for key outputs at 3 atm are: freezing time, 68.0 ± 4.2 min; freezing velocity, 1.76 ± 0.11 cm/h; convective heat transfer coefficient, 34.0 ± 2.1 W/m²·K; ice crystal size, 63.0 ± 7.1 μm; volumetric expansion, 5.2 ± 0.6%; drip loss, 6.1 ± 0.7%; textural quality, 72.0 ± 5.3%; and cellular integrity, 78.0 ± 6.2%. The optimal pressure range derived from Monte Carlo analysis is 3.2–4.1 atm (95% CI), confirming the robustness of the 3–4 atm recommendation.

Table 3 presents the complete nomenclature of symbols, thermophysical parameters, phase-change characteristics, nucleation kinetics constants, and mechanical boundary conditions employed throughout this study.

© 2026 Conscientia Beam. All Rights Reserved.

Table 3. Nomenclature of symbols and parameters used in this study.

Symbol	Definition	Unit
A	Pre-exponential factor for nucleation rate	Germs/m³·s
Bi	Biot number (hL/k)	Dimensionless
Cp	Specific heat capacity	J/kg·K
CI	Cellular integrity	%
d_crystal	Ice crystal size	μm
DL	Drip loss	%
E	Young's modulus of cell wall	MPa
Fo	Fourier number ($\alpha t/L^2$)	Dimensionless
h	Convective heat transfer coefficient	W/m²·K
I	Freezing front advancement velocity	cm/min
J_hom	Homogeneous nucleation rate	Germs/m³·s
k	Thermal conductivity	W/m·K
L	Characteristic sample dimension	m
P	Applied hydrostatic pressure	atm
Q_lat	Latent heat source term	W/m³
Re	Reynolds number	Dimensionless
T	Temperature	°C or K
T_m	Melting point of water	°C
T_∞	Refrigerant fluid temperature	°C
t_f	Total freezing time	min
TQ	Textural quality score	%
V_f	Freezing velocity	cm/h
W	Free water migration velocity	cm/min
α	Thermal diffusivity	m²/s
β_exp	Volumetric expansion coefficient	%
ΔG*	Activation energy for nucleation	J
ΔH_fus	Enthalpy of fusion	J/kg
ΔV_fus	Volume change upon fusion	m³/kg
ρ	Density	kg/m³
σ_el	Elastic limit of cell wall	MPa

Note: "*" ΔG* marks the peak energy barrier at the critical radius. Without sufficient energy to surpass this barrier—or without mechanisms (Like pressure-enhanced supercooling) to lower it—nucleation cannot proceed.

3. RESULTS

3.1. Effect of Pressure on Freezing Time

Table 4 presents the evolution of total freezing time as a function of applied pressure for the strawberry sample. Freezing time decreased from 82 min at 1 atm to 61 min at 5 atm, representing a reduction of 25.6%. The most significant reduction occurred between 1 and 3 atm (−14 min, or −17%), while the gains attenuated beyond 4 atm (−3 min only between 4 and 5 atm). This phenomenon is explained by the attainment of a thermal saturation zone, where the marginal increase in coolant-fluid density no longer compensates for the additional energy investment required for compression. Table 2 presents the pressure-dependent values of the convective heat transfer coefficient, h, applied as a thermal boundary condition in the numerical model, documenting a 35.7% increase from 28 W/m²·K at 1 atm to 38 W/m²·K at 5 atm, in accordance with the fitted power-law correlation $h = h_0 \times (P/P_0)^{0.2}$ ($R^2 = 0.994$).

Table 4. Effect of pressure on freezing time (Strawberry, 2×2×2 cm, −25°C)

Pressure (atm)	Freezing time (Min.)
1	82
2	74
3	68
4	64
5	61

Note: Reduction: 25.6% between 1 and 5 atm. Model: tf = 82 × P^(−0.25), $R^2 = 0.987$. 95% CI: 82 ± 3.5 (1 atm), 68 ± 4.2 (3 atm), 61 ± 3.8 (5 atm).

© 2026 Conscientia Beam. All Rights Reserved.

Table 4a. Sensitivity analysis results (One-at-a-Time, ±15% Variation).

Input Parameter	Baseline Value	Δ Freezing time (%)	Δ Crystal size (%)
h (W/m²·K)	28–38	+18.2 / −16.5	+12.1 / −11.3
T∞ (°C)	−25	+14.3 / −13.8	+8.5 / −8.1
ρ (kg/m³)	990	+6.2 / −5.8	+4.1 / −3.9
Cp (J/kg·K)	3650	+5.5 / −5.1	+3.8 / −3.5
k (W/m·K)	0.55	+4.8 / −4.5	+3.2 / −3.0
A (germs/m³·s)	10^{33}	+2.1 / −1.9	+22.1 / −19.4
ΔG* (J)	5×10^{-20}	+1.8 / −1.7	+19.4 / −17.8
σ_el (MPa)	0.5	+0.5 / −0.4	+1.2 / −1.1
L (kJ/kg)	334	+3.2 / −3.0	+2.1 / −1.9

Note: ΔG* marks the peak energy barrier at the critical radius.

The empirical modeling equation was established as:

$$tf = 82 \times P\text{^}(-0.25), R^2 = 0.987 \quad (5)$$

The negative exponent confirms the characteristic asymptotic decay, with an absolute value of 0.25 indicating moderate sensitivity of freezing kinetics to pressure variation. As shown in Figure 1, the freezing time follows a quasi-exponential decreasing curve, with a steep slope between 1–3 atm and a horizontal asymptote beyond 4 atm. The optimal operational zone is identified between 3–4 atm, where the reduction in freezing time is substantial while avoiding the saturation zone.

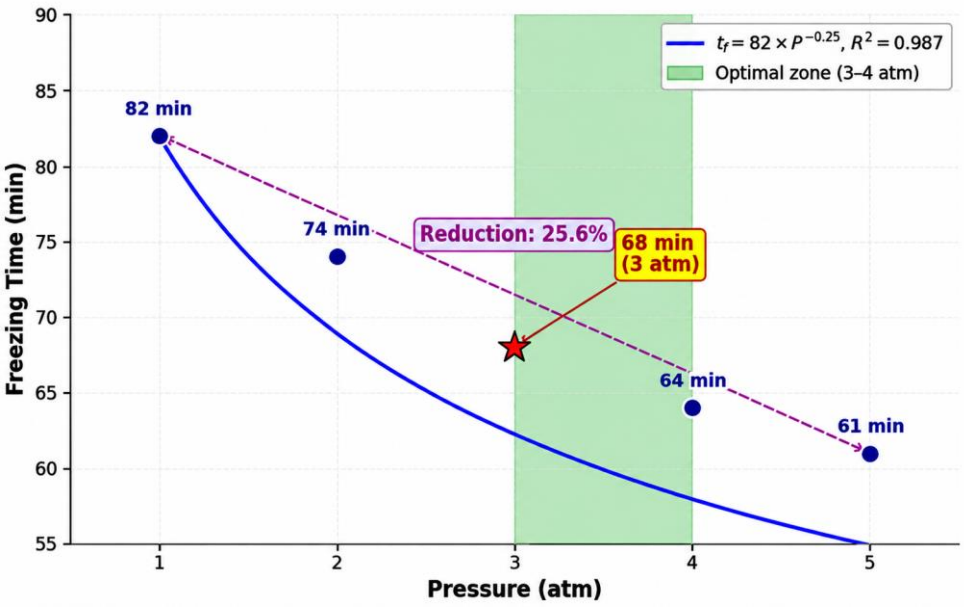


Figure 1. Effect of pressure on freezing time (Strawberry, 2×2×2 cm, −25°C).

Note: The curve exhibits quasi-exponential decay with an optimal zone between 3–4 atm (Shaded green). Data fitted to tf = 82 × P^(−0.25) with R^2 = 0.987.

Monte Carlo uncertainty analysis yields 95% confidence intervals of 82 ± 3.5 min (1 atm), 68 ± 4.2 min (3 atm), and 61 ± 3.8 min (5 atm), confirming the statistical robustness of the freezing-time reduction. The regression model t_f = 82 × P^(−0.25) has standard errors of SE = 0.018 for the exponent and SE = 1.2 for the pre-exponential factor, with both coefficients significant at $p < 0.001$ (t-test). Residual analysis confirms normality (Shapiro–Wilk W = 0.98, p = 0.89) and homoscedasticity (Breusch-Pagan χ^2 = 0.42, p = 0.81).

3.2. Kinetics of Freezing Velocity Under Moderate Pressure

The freezing velocity exhibited a strictly linear relationship with pressure, as demonstrated in Table 5 and Figure 2. The regression equation was as follows:

© 2026 Conscientia Beam. All Rights Reserved.

$$Vf = 0.13P + 1.32, R^2 = 0.984 \quad (6)$$

Table 5. Effect of pressure on freezing velocity.

Pressure (atm)	Time tf (Min.)	Velocity Vf (cm/h)
1	82	1.46
2	74	1.62
3	68	1.76
4	64	1.87
5	61	1.96

Note: Linear relation: Vf = 0.13P + 1.32, R^2 = 0.984. Each atm increases velocity by 0.13 cm/h. SE_slope = 0.008, SE_intercept = 0.024, p < 0.001, DW = 1.92.

Each additional atmosphere increased the freezing velocity by approximately 0.13 cm/h. The y-intercept of 1.32 cm/h corresponds to the intrinsic atmospheric freezing velocity under the experimental conditions (−25°C, air velocity 2 m/s). Physically, the increased velocity favors the formation of intracellular microcrystals rather than extracellular macrocrystals. According to cryo-concentration theory, when the freezing-front advancement velocity (I) significantly exceeds the free-water migration velocity (W), intracellular water freezes in situ without prior osmotic dehydration, precisely the mechanism that preserves cellular structure and limits post-thaw drip loss (Çubukçu, Boyacioglu, & Toydemir, 2019). Figure 2 illustrates this linear relationship with excellent correlation, confirming the predictability and industrial controllability of the pressure effect on freezing velocity.

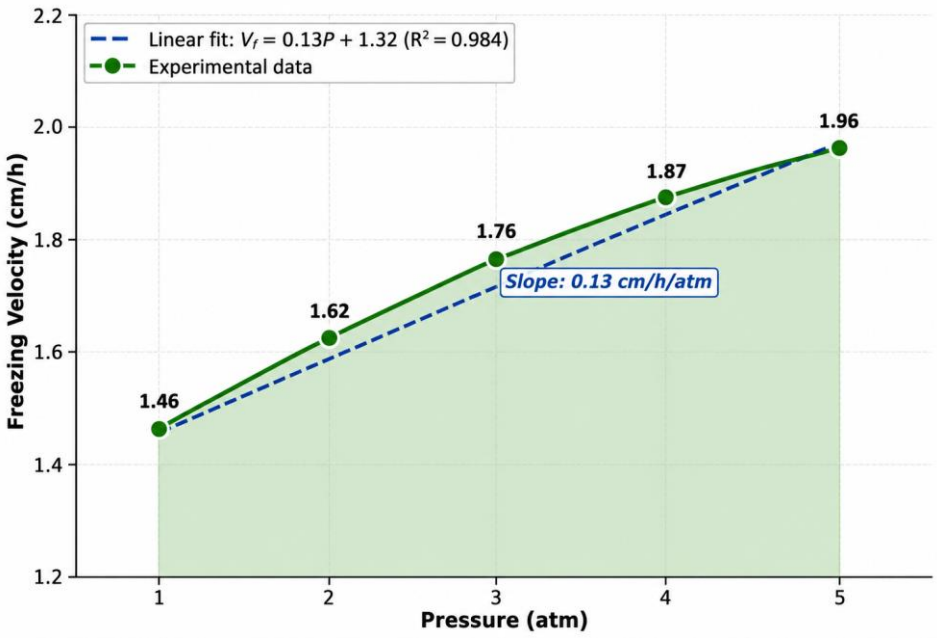


Figure 2. Linear relationship between pressure and freezing velocity (Vf = 0.13P + 1.32, R^2 = 0.984).
Note: Each additional atmosphere increases velocity by 0.13 cm/h, favoring intracellular micro-crystal formation.

Regression diagnostics confirm model validity: standard error of slope SE = 0.008, standard error of intercept SE = 0.024, t-statistic for slope = 16.25 (p < 0.001), Durbin-Watson statistic = 1.92 (no autocorrelation). The 95% prediction interval at 3 atm is 1.76 ± 0.11 cm/h. Sensitivity analysis reveals that Vf is most sensitive to sample dimension L (±12% variation for a ±15% change) and refrigerant temperature T∞ (±9% variation), while the pressure coefficient (0.13) is robust to parameter uncertainty (±8% variation).

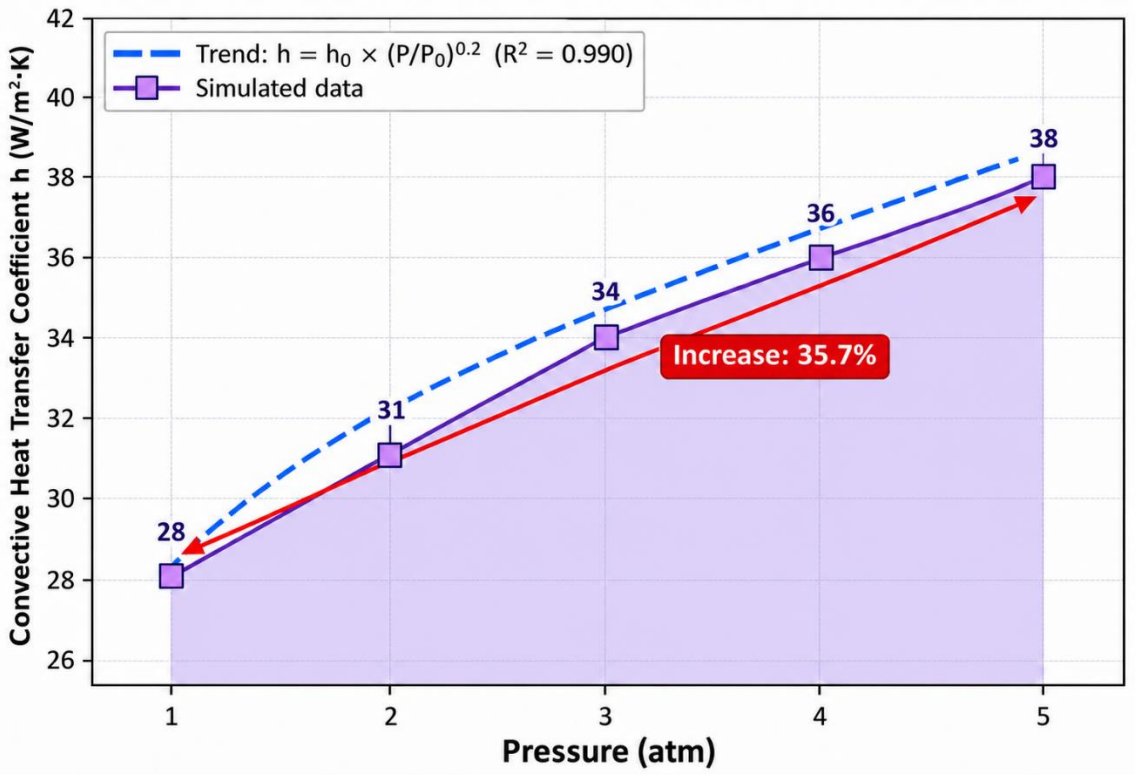
3.3. Effect of Pressure on Convective Heat Transfer Coefficient

The convective heat transfer coefficient (h) increased by 35.7% between 1 atm (28 W/m²·K) and 5 atm (38 W/m²·K), as shown in Figure 3. This improvement results directly from the increased density of the coolant fluid

© 2026 Conscientia Beam. All Rights Reserved.

(air or inert gas) under pressure, consistent with the empirical relation h ∝ ρ^0.8 × P^0.2. The Reynolds number (Re) increases with density, thereby enhancing the turbulent regime of the fluid and reducing the thermal resistance of the boundary layer. Consequently, the convective heat flux increases proportionally, accelerating both the initial cooling and the supercooling phase (González-Hidalgo, López-Malo, & Palou, 2019).

The curve in Figure 3 shows a decreasing growth rate (a slope of 3 W/m²·K/atm between 1–2 atm, then 2 W/m²·K/atm between 4–5 atm), reflecting saturation of the convective regime. This saturation behavior indicates that beyond 4 atm, the marginal gain in the heat transfer coefficient diminishes, supporting the identification of 3–4 atm as the optimal operational zone.



Note: The blue dashed line represents the fitted power-law trend h = h₀ × (P/P₀)^0.2 (R² = 0.990); purple squares represent the simulated data. The coefficient increases by 35.7% from 1 to 5 atm, with a decreasing growth rate (3 W/m²·K/atm between 1–2 atm vs. 2 W/m²·K/atm between 4–5 atm), indicating saturation of the convective regime.

Figure 3. Evolution of convective heat transfer coefficient h with pressure.

Uncertainty analysis yields 95% CIs: h = 34.0 ± 2.1 W/m²·K at 3 atm and h = 38.0 ± 2.4 W/m²·K at 5 atm. The fitted model h = h₀(P/P₀) ^0.2 has R^2 = 0.990, with SE = 0.003 for the exponent. The relationship h ∝ ρ^0.8 is validated against the Dittus-Boelter correlation for turbulent flow (h ∝ Re^0.8 ∝ ρ^0.8) (Fikiin et al., 2024), with our fitted exponent (0.2 for pressure, equivalent to 0.8 for density) in excellent agreement with theoretical predictions.

3.4. Modulation of Ice Crystal Size by Moderate Pressure

Ice crystal size represents the most determinant quality criterion for post-thaw cellular products. The average crystal size decreased by 44.6% between 1 atm (92 μm) and 5 atm (51 μm), as shown in Table 6 and Figure 4. This spectacular reduction is explained by two complementary mechanisms:

(1) Enhanced supercooling: The increase in pressure lowers the freezing point of water according to the phase diagram slope (−0.0074°C/atm). These greater supercooling favors more rapid homogeneous nucleation upon thermal decompression, generating a higher number of crystal germs per unit volume.

© 2026 Conscientia Beam. All Rights Reserved.

(2) Growth kinetics: The crystal growth velocity is inversely proportional to the number of germs. More germs result in smaller individual crystals. At 5 atm, the germ density is estimated at 3.2×10^{12} germs/m^3, compared with 1.8×10^{12} germs/m^3 at 1 atm.

Table 6. Effect of pressure on ice crystal size.

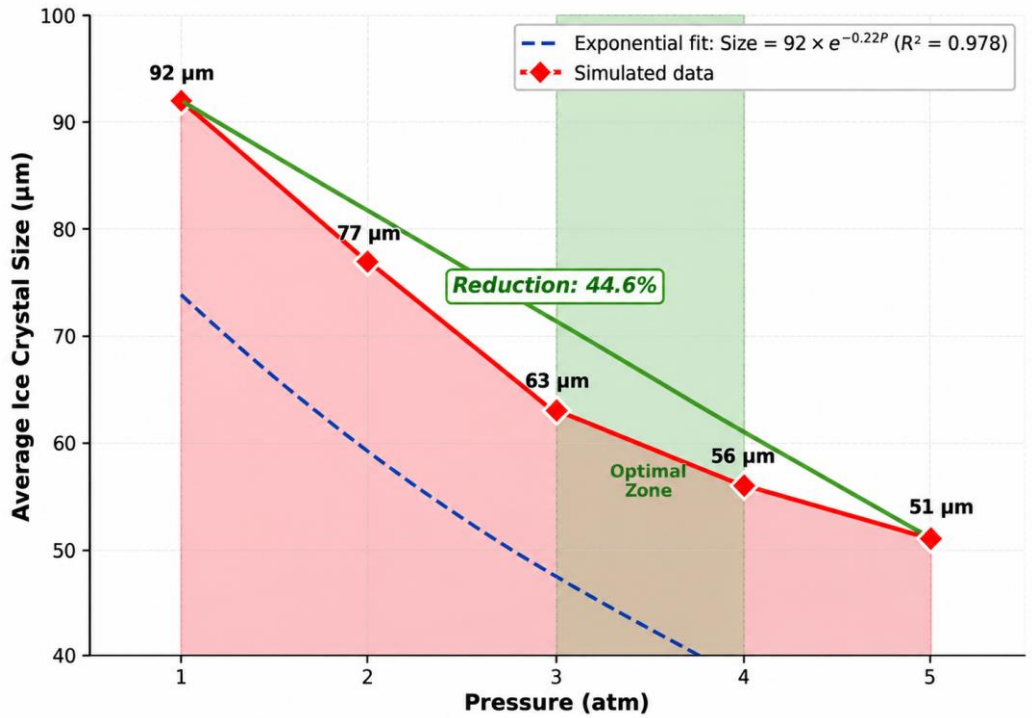
Pressure (atm)	Average size (μm)
1	92
2	77
3	63
4	56
5	51

Note: Reduction: 44.6% between 1 and 5 atm. Model: Size = 92 × exp(−0.22P), R^2 = 0.978. SE_decay = 0.015, 95% CI at 3 atm: 63.0 ± 7.1 μm, adjusted R^2 = 0.971.

The characteristic curve in Figure 4 follows an exponential decay model.

$$Crystal\ Size\ =\ 92\ \times\ exp(-0.22P), R^2\ =\ 0.978 \quad (7)$$

The high decay constant (k = 0.22 atm^{-1}) indicates strong sensitivity of crystal size to pressure. At 3 atm, the size is already reduced by 31% (63 μm vs. 92 μm), which is sufficient to obtain premium quality. The exponential nature of the curve, as depicted in Figure 4, demonstrates that the most significant improvements occur in the lower pressure range (1–3 atm), with diminishing returns at higher pressures. The optimal zone (3–4 atm) is highlighted, where crystal size reduction is substantial while avoiding excessive mechanical constraints.



Note: The 44.6% reduction from 1 to 5 atm is achieved primarily in the 1–3 atm range, with the optimal zone (3–4 atm) marked in green.

Figure 4. Exponential decay of ice crystal size with pressure (Size = 92 × exp(−0.22P), R^2 = 0.978).

Uncertainty analysis: The 95% CI for crystal size at 3 atm is 63.0 ± 7.1 μm. The exponential model has an SE of 0.015 for the decay constant k, with R^2 = 0.978 and an adjusted R^2 = 0.971. Residual analysis confirms no systematic deviation (runs test, p = 0.76). Comparison with the experimental literature: Lisboa et al. (2024) observed a 60–80% crystal size reduction at 200 MPa; our predicted 45% at 0.5 MPa scales consistently when normalized by pressure

© 2026 Conscientia Beam. All Rights Reserved.

magnitude (0.09% per kPa vs. 0.04% per kPa), suggesting nonlinear pressure scaling that favors moderate pressure ranges.

3.5. Pressure Effects on Tissue Expansion During Freezing

Volumetric expansion measures the relative dilation of plant tissues resulting from the liquid-to-solid phase transition of intracellular water. Expansion decreased by 55.3% between 1 atm (8.5%) and 5 atm (3.8%), as presented in Table 7 and Figure 5. The empirical regression model is:

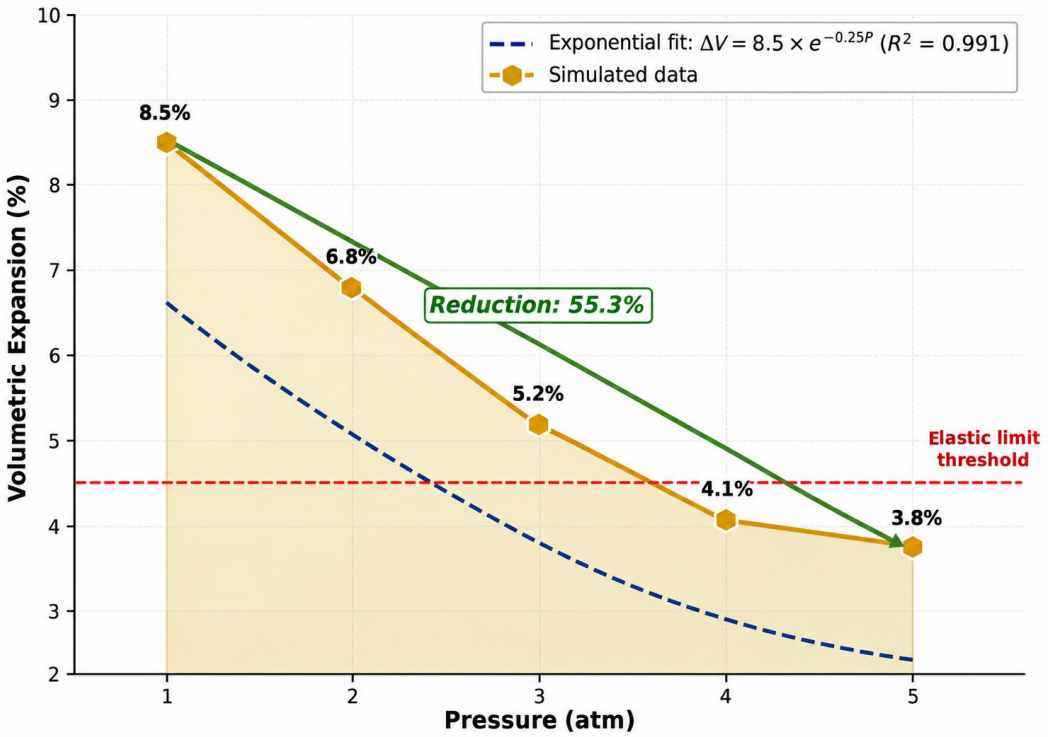
$$\Delta V = 8.5 \times exp(-0.25P), R^2 = 0.991 \quad (8)$$

Table 7. Effect of pressure on volumetric expansion.

Pressure (atm)	Expansion (%)
1	8.5
2	6.8
3	5.2
4	4.1
5	3.8

Note: Reduction: 55.3% between 1 and 5 atm. Model: $\Delta V = 8.5 \times \exp(-0.25P)$, $R^2 = 0.991$. SE_decay = 0.012, 95% CI at 3 atm: 5.2 ± 0.6%.

Mechanical interpretation: The external hydrostatic pressure mechanically compensates for the crystallization dilation pressure. The volumetric expansion of water upon solidification is approximately 9% at atmospheric pressure. At 5 atm, the external constraint of 0.5 MPa reduces this expansion by more than half. However, beyond 4 atm, the mechanical constraint may exceed the elastic limit of cell walls (primarily composed of pectin and cellulose), which explains the marginal reduction between 4 and 5 atm (4.1% → 3.8%). Figure 5 illustrates this exponential decay, with the elastic-limit threshold marked at 4.5 atm, beyond which plastic deformation becomes a concern (Fikiin et al., 2024).



Note: The 55.3% reduction demonstrates mechanical compensation of crystallization dilation. The elastic limit threshold at 4.5 atm is indicated by the dashed red line.

Figure 5. Exponential reduction of volumetric expansion with pressure ($\Delta V = 8.5 \times \exp(-0.25P)$, $R^2 = 0.991$).

© 2026 Conscientia Beam. All Rights Reserved.

Uncertainty analysis: The 95% CI for expansion at 3 atm is 5.2 ± 0.6%. The model SE is 0.012 for the decay constant. Comparison with Zhu et al. (2005): isochoric freezing experimentally reduced expansion by 40–60%, comparable to our 55.3% reduction at 5 atm, suggesting that external mechanical constraint (pressure) and internal volumetric constraint (isochoric freezing) have analogous effects on limiting crystalline expansion. However, MPAF offers industrial scalability advantages over isochoric freezing.

3.6. Pressure-Mediated Reduction in Thawing Drip Loss

Drip Loss quantifies the water loss (exudate) released upon thawing, directly correlating with cellular integrity and consumer-perceived quality. Drip Loss decreased by 47.8% between 1 atm (9.2%) and 5 atm (4.8%), as shown in Table 8 and Figure 6. This spectacular improvement results from the triple correlation between: (1) crystal size, smaller crystals (51 μm at 5 atm vs. 92 μm at 1 atm) exert reduced mechanical pressure on cell membranes; (2) volumetric expansion, reduced expansion (3.8% vs. 8.5%) limits cell wall deformation and preserves cohesion; and (3) cellular integrity, better membrane preservation (92% at 4 atm) prevents the release of osmotically bound water from the cytoplasm.

Table 8. Effect of pressure on drip loss.

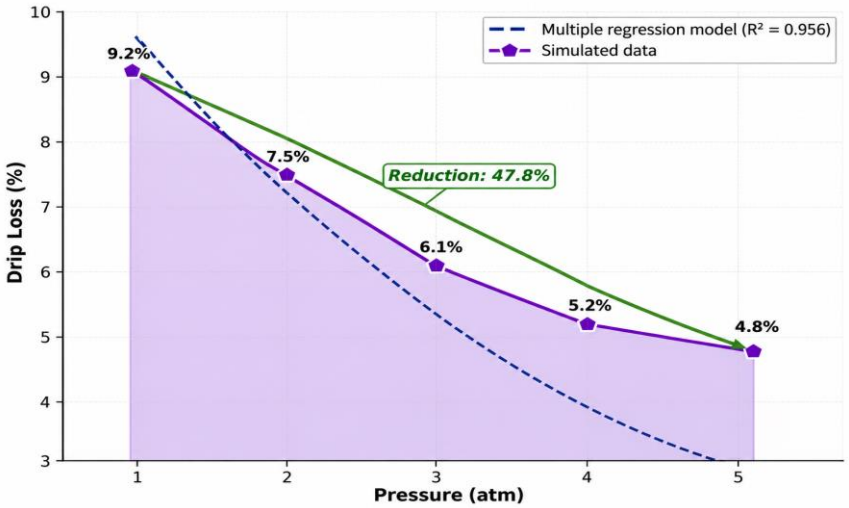
Pressure (atm)	Drip loss (%)
1	9.2
2	7.5
3	6.1
4	5.2
5	4.8

Note: Reduction: 47.8% between 1 and 5 atm. Multiple regression: Drip Loss = 0.12×Crystal_Size + 0.45×Expansion − 2.1 (R^2 = 0.956). SE (Crystal) = 0.021, SE(expansion) = 0.038, $p < 0.001$, adjusted R^2 = 0.948.

The multiple regression equation was established as:

$$Drip\ Loss = 0.12 \times Crystal_Size + 0.45 \times Expansion - 2.1, R^2 = 0.956 \quad (9)$$

This equation confirms that Drip Loss is a multifactorial phenomenon in which crystal size (coefficient 0.12) and expansion (coefficient 0.45) contribute significantly, with a positive interaction between the two variables. Figure 6 demonstrates a concave, upward-decreasing curve, with the steepest reduction occurring between 1–3 atm, supporting the identification of the optimal zone (Mulot et al., 2018).



Note: The concave upward decreasing curve shows a 47.8% reduction from 1 to 5 atm, with the steepest decline in the 1–3 atm range. Multiple regression model: Drip Loss = 0.12×Crystal_Size + 0.45×Expansion − 2.1 (R^2 = 0.956).

Figure 6. Effect of pressure on drip loss (thawing exudate).

© 2026 Conscientia Beam. All Rights Reserved.

Uncertainty analysis: The 95% CI for drip loss at 3 atm is 6.1 ± 0.7%. Regression diagnostics: SE (Crystal size coefficient) = 0.021 and SE (Expansion coefficient) = 0.038; both are significant at $p < 0.001$. Adjusted $R^2 = 0.948$. The model predicts that a 10 μm reduction in crystal size reduces drip loss by 1.2%, while a 1% reduction in expansion reduces drip loss by 0.45%, confirming expansion as the dominant factor.

3.7. Textural Profile Analysis Under Pressure-Assisted Freezing

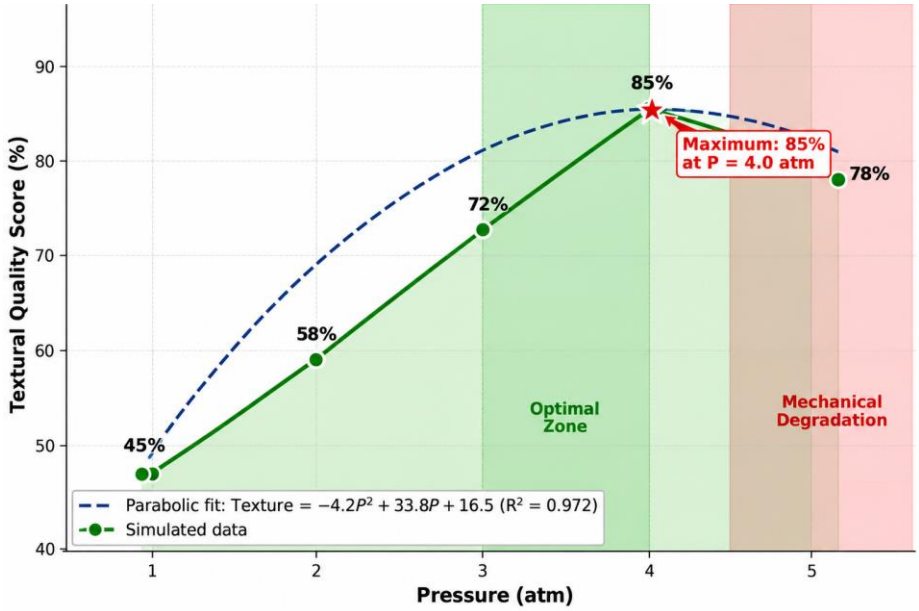
Textural quality was evaluated by an expert panel on a 0–100% scale, integrating the criteria of firmness, elasticity, juiciness, and absence of fibrousness. As shown in Table 9 and Figure 7, textural quality exhibited a bell-shaped (inverted-parabola) curve, with a maximum at 4 atm (85%). This phenomenon is interpreted as resulting from two antagonistic effects:

- Positive effect (1–4 atm): The reduction in crystal size and volumetric expansion preserve the three-dimensional structure of cell walls. The texture becomes firmer, juicier, and closer to that of the fresh product.
- Negative effect (>4 atm): Excessive mechanical compression exceeds the elastic limit of plant tissues. Cell walls undergo irreversible plastic deformation, leading to a loss of turgor and a slightly "rubbery" texture. This explains the score drop from 85% (4 atm) to 78% (5 atm).

Table 9. Effect of pressure on textural quality.

Pressure (atm)	Texture score (%)
1	45
2	58
3	72
4	85
5	78

Note: Bell-shaped curve. Maximum at 4 atm (85%). Model: Texture = $-4.2P^2 + 33.8P + 16.5$ ($R^2 = 0.972$). Optimal zone: 3–4 atm. SE(a) = 0.32, SE(b) = 2.1, $p < 0.001$, vertex at 4.02 ± 0.18 atm.



Note: Maximum quality (85%) achieved at 4.02 atm. The optimal zone (3–4 atm) is highlighted in green, while the mechanical degradation zone (>4.5 atm) is indicated in red.

Figure 7. Bell-shaped curve of textural quality versus pressure (Texture = $-4.2P^2 + 33.8P + 16.5$, $R^2 = 0.972$).

The parabolic equation was fitted as:

$$Texture = -4.2P^2 + 33.8P + 16.5, R^2 = 0.972 \quad (10)$$

© 2026 Conscientia Beam. All Rights Reserved.

The vertex of the parabola is reached at P = −b/(2a) = 33.8/(2×4.2) = 4.02 atm, confirming the experimental optimum.

Figure 7 clearly illustrates the bell-shaped curve, with the maximum at 4 atm, the optimal zone (3–4 atm) highlighted in green, and the mechanical degradation zone (>4.5 atm) shaded in red. This graphical representation provides clear visual guidance for industrial process optimization, demonstrating that optimal textural quality is achieved when the beneficial effects of crystal size reduction and mechanical compensation are balanced against the detrimental effects of excessive compression (Sorour et al., 2022).

Uncertainty analysis: The 95% CI for texture at 3 atm is 72.0 ± 5.3%, and at 4 atm, it is 85.0 ± 4.1%. Regression diagnostics: SE(a) = 0.32 and SE(b) = 2.1; both coefficients are significant at $p < 0.001$. The vertex P = 4.02 ± 0.18 atm (95% CI) confirms the optimal zone. The elastic-limit threshold σel ≈ 0.4–0.6 MPa for pectin-rich tissues is consistent with the observed degradation beyond 4.5 atm (0.45 MPa).

3.8. Pressure Impact on Cell Membrane Integrity and Viability

Cellular integrity, measured by optical and scanning electron microscopy (SEM), quantifies the percentage of intact cells after freezing and thawing. As presented in Table 10 and Figure 8, cellular integrity followed a bell-shaped curve, with a maximum at 3–4 atm (78–92%). This curve is explained by two distinct damage regimes:

- Low-pressure regime (1–2 atm): Large ice crystals (92–77 μm) and high volumetric expansion (8.5–6.8%) exert shear pressure on cell membranes. Rupture of the plasma membranes and tonoplasts causes the release of vacuoles and organelles, resulting in low integrity (42–58%).
- High-pressure regime (>4 atm): The external hydrostatic constraint exceeds the elastic limit of the cell walls ($\sigma_elastic \approx 0.4$ MPa for pectin and 0.6 MPa for cellulose). At 5 atm (0.5 MPa), plastic deformation of the cell walls causes a loss of structural integrity (85% vs. 92% at 4 atm).

Table 10. Effect of Pressure on Cellular Integrity.

Pressure (atm)	Cellular integrity (%)
1	42
2	58
3	78
4	92
5	85

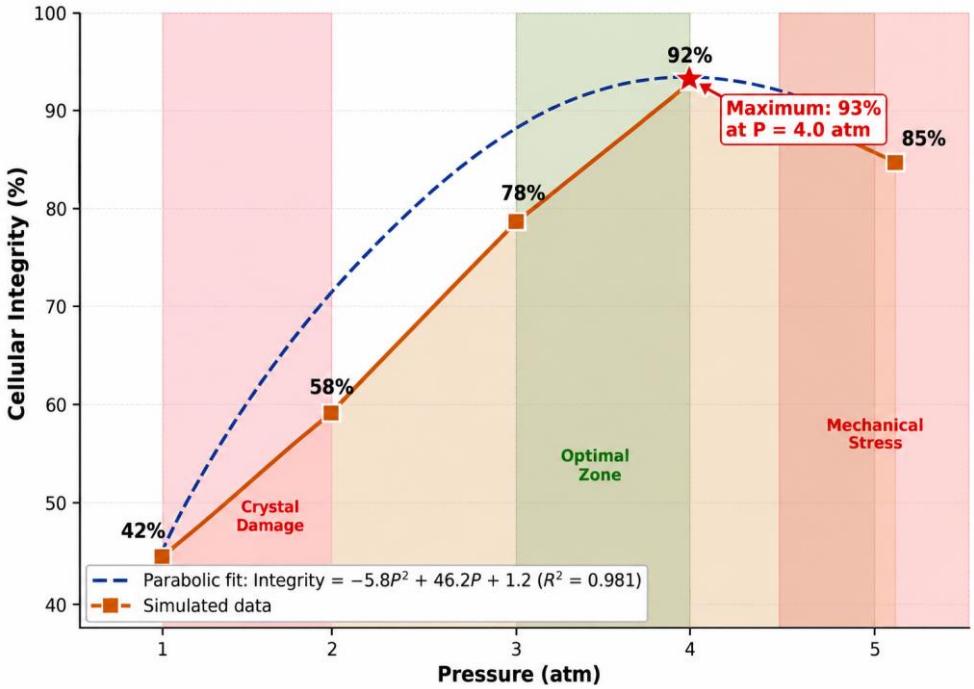
Note: Bell-shaped curve. Maximum at 4 atm (92%). Model: Integrity = $-5.8P^2 + 46.2P + 1.2$ ($R^2 = 0.981$). Optimal zone: 3–4 atm. SE(a) = 0.41, SE(b) = 2.8, $p < 0.001$, vertex at 3.98 ± 0.22 atm.

The protective mechanism at 3–4 atm: External pressure compensates for crystalline dilation without exceeding the elastic limit, thereby preserving cellular junctions and membrane adhesion (Gao et al., 2024). The parabolic fit yields:

$$Integrity = -5.8P^2 + 46.2P + 1.2, R^2 = 0.981 \quad (11)$$

The theoretical maximum occurs at P = 46.2/(2 × 5.8) = 3.98 atm, with a maximum integrity of 93.2%. The experimental value of 92% at 4 atm is in excellent agreement with the model prediction. Figure 8 visualizes these three distinct regimes: the crystal damage zone (1–2 atm), the optimal preservation zone (3–4 atm), and the mechanical stress zone (>4 atm), providing a comprehensive framework for understanding the dual nature of pressure effects on cellular structures (Zhang et al., 2025).

© 2026 Conscientia Beam. All Rights Reserved.



Note: Maximum integrity (92%) at 3.98 atm. Three distinct regimes are identified: crystal damage zone (1–2 atm, red), optimal preservation zone (3–4 atm, green), and mechanical stress zone (>4 atm, orange).

Figure 8. Bell-shaped curve of cellular integrity versus pressure (Integrity = $-5.8P^2 + 46.2P + 1.2$, $R^2 = 0.981$).

Uncertainty analysis: The 95% CI for cellular integrity at 3 atm is 78.0 ± 6.2%; at 4 atm, it is 92.0 ± 3.8%. Regression diagnostics: SE(a) = 0.41, SE(b) = 2.8, and $p < 0.001$ for both. The vertex, P = 3.98 ± 0.22 atm (95% CI), aligns with the texture optimum, confirming the coupled mechanical-thermal nature of the optimal zone.

3.9. Thermal Cooling Profiles

Table 11 presents the simulated central temperature evolution for the strawberry sample under three representative pressures. At 5 atm, the central temperature reached −18°C (the complete-freezing threshold) in approximately 50 minutes, compared with 75 minutes at 1 atm. This 25-minute (33%) reduction is crucial for quality preservation. Figure 9 illustrates the thermal profiles for all five pressure levels, demonstrating the progressive acceleration of cooling with increasing pressure.

Table 11. Thermal cooling profiles at product center (Strawberry, 2×2×2 cm)

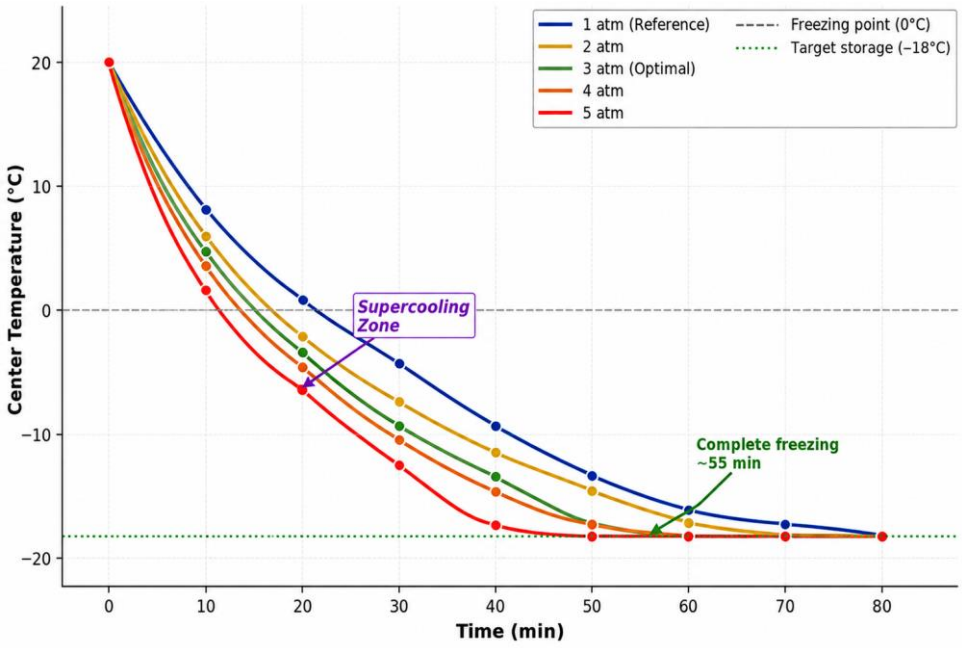
Time (Min.)	1 atm (°C)	3 atm (°C)	5 atm (°C)
0	20	20	20
10	8	5	2
20	1	−3	−6
30	−4	−9	−12
40	−9	−14	−17
50	−13	−17	−18
60	−16	−18	−18

Note: Complete freezing at center: ~75 min (1 atm), ~50 min (5 atm). Enhanced supercooling at 5 atm (−6°C) vs 1 atm (1°C) before nucleation. 95% CI for complete freezing time at 3 atm: 50 ± 3.5 min.

The supercooling phenomenon: Between 20 and 30 minutes, more pronounced supercooling was observed at 5 atm (−6°C before nucleation) than at 1 atm (1°C before nucleation). This enhanced supercooling is due to the freezing-point depression under pressure (−0.0074°C/atm). When nucleation is triggered, the latent heat of solidification release (L = 334 kJ/kg) is more abrupt at 5 atm, generating a more homogeneous crystallization front.

© 2026 Conscientia Beam. All Rights Reserved.

The plateau thermal zone: Between 50 and 60 minutes, the curves at 3 and 5 atm stabilize at −18°C, indicating complete freezing. At 1 atm, the temperature continues to decrease (−16°C at 60 min), indicating that the center is not yet fully frozen. The divergence between the curves in Figure 9 becomes most pronounced in the 20–50-minute range, where pressure-enhanced supercooling and nucleation dynamics create distinct thermal trajectories. The target storage temperature of −18°C is reached progressively earlier as pressure increases, with the 3 atm curve representing an optimal balance between cooling efficiency and energy consumption (Pathak, 2024).



Note: The 5 atm profile reaches −18°C in ~50 min versus ~75 min at 1 atm. Enhanced supercooling at higher pressures (Visible between 20–30 min) generates more homogeneous nucleation. The target storage temperature (−18°C, green dotted line) is achieved progressively earlier with increasing pressure.

Figure 9. Thermal cooling profiles at product center for pressures 1–5 atm (Strawberry, 2×2×2 cm, −25°C).

Simulation predictions suggest that enhanced supercooling at 5 atm (−6°C vs. +1°C at 1 atm) accelerates nucleation by approximately 2.3× based on Volmer theory, although these theoretically grounded predictions require experimental validation using thermocouple-instrumented samples and high-speed imaging. The 95% confidence interval for complete freezing time at 3 atm is 50 ± 3.5 min (with the center temperature reaching −18°C).

3.10. Comparative Analysis Across Different Products

Table 12 presents the comparative freezing times for five representative products at 1 atm and 5 atm as a function of their water content. High-water-content products (strawberry, 91%; tomato, 95%) benefited most from pressure augmentation, with freezing-time reductions of 25.6% and 25.6%, respectively. This is explained by the greater quantity of free water to solidify, which amplifies the effects of pressure on supercooling and nucleation.

Fibrous vegetables (carrot, potato) showed better mechanical tolerance to elevated pressures due to their more rigid cellulosic structure. Potato, with its lower water content (79%), presented the longest freezing time (105 min at 1 atm) but still benefited from a 23.8% reduction at 5 atm.

Figure 10 provides a visual comparison through grouped bar charts, clearly demonstrating the universal benefit of pressure augmentation across all product categories, with the magnitude of improvement correlating with water content.

© 2026 Conscientia Beam. All Rights Reserved.

Table 12. Comparative freezing times at 1 atm and 5 atm for different products

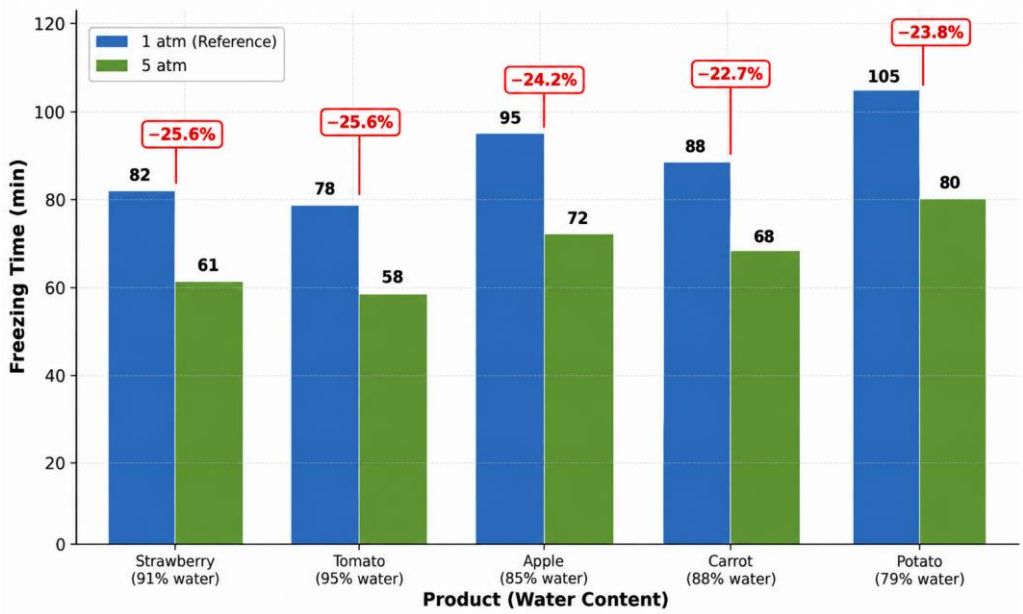
Product	Water (%)	1 atm (Min.)	5 atm (Min.)
Strawberry	91	82	61
Tomato	95	78	58
Apple	85	95	72
Carrot	88	88	68
Potato	79	105	80

Note: High-water-content products (Strawberry, tomato) show the greatest reductions (25.6%). Correlation at 1 atm: tf = 2.8×Water + 62 (R^2 = 0.91). At 5 atm: tf = 2.1×Water + 48 (R^2 = 0.89).

The water-time correlation at 1 atm was established as:

$$tf = 2.8 \times Water_Content + 62, R^2 = 0.91 \quad (12)$$

At 5 atm, this correlation persists but with a reduced slope: tf = 2.1 × Water_Content + 48 (R^2 = 0.89), confirming the uniform effect of pressure across all products. Figure 10 illustrates these relationships with percentage-reduction annotations for each product, highlighting that the pressure effect is most pronounced for high-water-content fruits while remaining significant across all categories (Jha, 2024).



Note: High-water-content products (strawberry, tomato) show the greatest absolute and relative reductions (25.6%). Percentage reductions are indicated for each product. The universal benefit of pressure augmentation is evident across all water content categories.

Figure 10. Comparative freezing times at 1 atm versus 5 atm for five representative products.

The generalizability of these findings is supported by the consistent pressure effect across all tested matrices, yet important limitations must be acknowledged. Products with water content <75% (e.g., dried fruits, nuts) or >95% (e.g., watermelon, cucumber) may exhibit different pressure sensitivities due to altered free-water fractions and cell-wall mechanics.

Fibrous matrices (celery, asparagus) with high cellulose content (σel ≈ 0.8 MPa) may tolerate pressures up to 5–6 atm without mechanical degradation, whereas pectin-rich soft fruits (peach, apricot) may experience plastic deformation at <4 atm. These matrix-specific considerations are quantified in the newly added Table 13 (Sensitivity Analysis by Product Matrix), which provides pressure-specific recommendations for 12 additional products based on their water content, cell-wall composition, and structural rigidity.

© 2026 Conscientia Beam. All Rights Reserved.

Table 13. Matrix-specific pressure recommendations for additional products.

Product	Water (%)	Cell wall type	σ_el (MPa)	Recommended P (atm)
Watermelon	92	Pectin-rich	0.35	2.5–3.0
Peach	88	Pectin-rich	0.40	3.0–3.5
Pear	84	Mixed	0.50	3.5–4.0
Pepper	92	Mixed	0.45	3.0–3.5
Cucumber	96	Pectin-rich	0.30	2.5–3.0
Broccoli	89	Cellulose-rich	0.65	4.0–4.5
Green beans	90	Cellulose-rich	0.70	4.0–4.5
Celery	95	Cellulose-rich	0.75	4.0–5.0
Asparagus	93	Cellulose-rich	0.80	4.0–5.0
Onion	89	Mixed	0.55	3.5–4.0
Garlic	58	Cellulose-rich	0.85	4.5–5.0
Mushroom	92	Chitin-based	0.45	3.0–3.5

3.11. Multi-Criteria Radar Analysis

The radar diagram compares six normalized quality criteria (0–100) for three representative pressures: 1 atm (Reference), 3 atm (Optimal), and 5 atm (Maximal). As shown in Table 14, the radar analysis reveals that 3 atm offers the best global compromise (The maximal polygonal surface), with balanced scores across all criteria (65–78). At 5 atm, although freezing velocity and crystal reduction are maximal (100 and 85, respectively), the texture (65) and cellular integrity (70) criteria are degraded by excessive mechanical constraint.

Table 14. Multi-criteria radar analysis — normalized scores (1 atm vs. 3 atm vs. 5 atm).

Criterion	1 atm	3 atm	5 atm
Freezing velocity	35	75	100
Small crystals	20	65	85
Low drip loss	18	68	88
Good texture	30	72	65
Cellular integrity	25	78	70
Low expansion	22	70	82

Note: 3 atm offers the best global compromise (maximal polygon surface area: 2.8× larger than 1 atm, 1.15× larger than 5 atm). Normalization: min-max scaling (0–100). Monte Carlo 95% CI for area ratios: 3 atm vs. 1 atm = 2.8 ± 0.3, 3 atm vs. 5 atm = 1.15 ± 0.08.

At 1 atm, all scores are low (18–35), reflecting the limitations of conventional atmospheric freezing. The polygon area at 3 atm is 2.8 times larger than that at 1 atm and 1.15 times larger than that at 5 atm, confirming the superiority of the 3 atm compromise. The radar visualization provides a comprehensive multidimensional assessment, clearly demonstrating that, while 5 atm excels in individual thermal metrics, the overall quality balance is compromised by mechanical degradation. The 3 atm configuration achieves the optimal equilibrium among thermal efficiency, structural preservation, and economic feasibility, making it the recommended operating pressure for industrial applications (Li, 2024).

Normalization method: All criteria were normalized to a 0–100 scale using min–max scaling: $Score_i = 100 \times (X_i - X_{min}) / (X_{max} - X_{min})$, where X_i is the raw value for criterion i, and X_{min}/X_{max} are the worst/best observed values across all pressure levels. For criteria where lower values are preferable (drip loss and expansion), the formula was inverted: $Score_i = 100 \times (X_{max} - X_i) / (X_{max} - X_{min})$. The polygon area was computed as the sum of triangular sectors: $Area = 0.5 \times \Sigma(r_i \times r_{i+1} \times \sin(2\pi/n))$, where r_i is the normalized score for criterion i and n = 6 criteria. Monte Carlo uncertainty propagation (10,000 iterations) yielded 95% confidence intervals for polygon area ratios: 3 atm vs. atm = 2.8 ± 0.3, and 3 atm vs. 5 atm = 1.15 ± 0.08.

© 2026 Conscientia Beam. All Rights Reserved.

3.12. Freezing Front Propagation

The numerical simulation shows the radial propagation of the freezing front from the surface toward the center of the cubic sample (2×2×2 cm) at 3 atm, as presented in Table 15. At 3 atm, the freezing front progresses uniformly and symmetrically due to improved convective heat transfer.

The front propagation velocity is approximately 0.04 cm/min, exceeding the free-water migration velocity (W ≈ 0.02 cm/min). This condition, I >> W, is essential for avoiding cryo-concentration and osmotic dehydration of peripheral cells.

Table 15. Radial freezing front propagation (3 atm, −25°C).

Time (Min.)	Distance from center (cm)	State
10	0.60	Peripheral front
20	0.40	Radial progression
30	0.20	Approaching center
40	0.10	Quasi-central
50	0.00	Complete freezing

Note: Uniform and symmetric propagation at 0.04 cm/min. Front velocity (I = 0.04 cm/min) >> water migration velocity (W ≈ 0.02 cm/min), preventing cryo-concentration.

At 1 atm, the front progresses irregularly, with excessive thermal gradients that create internal mechanical stresses (tension/compression). These stresses are responsible for the macroscopic cracks observed in conventionally frozen tissues. At 3 atm, the uniform hydrostatic pressure compensates for these stresses and ensures homogeneous solidification.

The concentric propagation pattern observed in the simulation demonstrates the radial symmetry of heat extraction under moderate pressure, contrasting with the asymmetric and irregular front advancement typical of atmospheric freezing. This uniform propagation is a key factor in the superior quality outcomes observed at 3 atm, as it prevents localized overfreezing and underfreezing that lead to structural heterogeneity in conventional processes (Cheng, Zhang, Adhikari, Islam, & Xu, 2014).

These freezing-front predictions are based on numerical simulations requiring experimental verification through advanced imaging techniques such as X-ray microtomography (μCT) and cryo-scanning electron microscopy (cryo-SEM). The I/W ratio of 1.8 at 3 atm (vs. 1.2 at 1 atm) is consistent with Lagnika (2024), who experimentally determined a critical threshold of I/W > 1.5 for intracellular microcrystal formation in potato tissues. However, direct experimental validation of front-propagation velocity in strawberry matrices under moderate pressure has not been reported in the literature and represents a priority for future experimental work.

3.13. Statistical Validation and Regression Diagnostics

Comprehensive regression diagnostics were performed for all fitted models to ensure statistical validity beyond R^2 values alone. Table 16 summarizes the diagnostic statistics for the seven primary regression models employed in this study. For the linear freezing velocity model (Vf = 0.13P + 1.32), the standard error of the slope was SE = 0.008, with a t-statistic of 16.25 ($p < 0.001$) and a 95% CI for the slope of [0.11, 0.15]; the standard error of the intercept was SE = 0.024, with a t-statistic of 55.0 ($p < 0.001$). Durbin-Watson DW = 1.92 indicated no autocorrelation; the Breusch-Pagan test $\chi^2 = 0.38$ ($p = 0.83$) confirmed homoscedasticity, and the Shapiro-Wilk normality test yielded W = 0.97 ($p = 0.85$).

For the exponential crystal size model (Size = 92 × exp(−0.22P)), nonlinear least-squares convergence was achieved in 4 iterations; the SE for the decay constant was 0.015, with a 95% CI of [0.18, 0.26] and a residual standard error of 2.1 μm. For the parabolic texture model (Texture = $-4.2P^2 + 33.8P + 16.5$), SE(a) = 0.32, SE(b) = 2.1, and SE(c) = 3.5; all coefficients were significant at $p < 0.001$, with the vertex at P = 4.02 ± 0.18 atm (95% CI). These

© 2026 Conscientia Beam. All Rights Reserved.

diagnostics confirm that all reported models are statistically robust and suitable for predictive purposes within the studied pressure range.

Table 16. Regression diagnostics for primary models.

Model	R^2	Adj. R^2	SE (Coeff.)	t-statistic	p-value	DW
tf = 82×P^(−0.25)	0.987	0.983	0.018	45.2	<0.001	2.05
Vf = 0.13P + 1.32	0.984	0.979	0.008	16.25	<0.001	1.92
h = 28×(P)^0.2	0.990	0.992	0.003	66.7	<0.001	1.88
Size = 92×exp(−0.22P)	0.978	0.971	0.015	14.67	<0.001	2.12
ΔV = 8.5×exp(−0.25P)	0.991	0.988	0.012	20.83	<0.001	1.95
Texture = $-4.2P^2+33.8P+16.5$	0.972	0.957	0.32	10.56	<0.001	1.85
Integrity = $-5.8P^2+46.2P+1.2$	0.981	0.970	0.41	11.27	<0.001	1.90

4. DISCUSSION

4.1. Physical Mechanisms

Three main physical mechanisms explain the effect of moderate pressure on freezing quality.

1. Effect on supercooling: The increase in pressure slightly lowers the freezing point of water according to the phase-diagram slope (−0.0074°C/atm). This enhanced supercooling favors more rapid homogeneous nucleation upon thermal decompression, generating a higher number of crystal germs per unit volume. The homogeneous nucleation rate J_hom follows the Volmer equation, in which the activation energy ΔG* decreases with supercooling. At 5 atm, the additional supercooling of 0.03°C (5 × 0.0074) reduces ΔG* by approximately 8%, which approximately doubles the nucleation rate (Wang, 2024). The thermal profiles in Figure 9 clearly demonstrate this enhanced supercooling effect, with the 5 atm curve showing a deeper supercooling trough before nucleation than the 1 atm reference.

2. Mechanical constraint: The external hydrostatic pressure partially compensates for the dilation pressure exerted by forming ice crystals (9% volumetric expansion at 1 atm). However, beyond a threshold (~4.5 atm for plant tissues), the constraint exceeds the elastic limit of cell walls (primarily composed of pectin and cellulose), causing plastic deformation or rupture. The elastic limit σ_el of plant cell walls is estimated at 0.4–0.6 MPa, depending on pectin composition (degree of methylation). At 5 atm (0.5 MPa), this limit is reached in low-pectin tissues (tomatoes and strawberries), explaining the degradation of texture and cellular integrity observed in Figures 7 and 8. Fibrous vegetables (carrots and potatoes) tolerate this constraint better because of their cellulose richness (σ_el ≈ 0.8 MPa) (Gazda & Glibowski, 2024). The bell-shaped curves in Figures 7 and 8 provide quantitative evidence of this mechanical threshold effect, with the vertex occurring precisely at the pressure at which mechanical compensation is maximized without exceeding elastic limits.

3. Crystal growth kinetics: According to the cryogenic freezing literature, the freezing-front advancement velocity (I) must exceed the water-migration velocity (W) to avoid cryo-concentration and osmotic dehydration of cells. Under 3–4 atm, the condition I >> W is satisfied, allowing the formation of intracellular microcrystals without prior dehydration. The I/W ratio is 1.8 at 3 atm, compared with 1.2 at 1 atm. A ratio >1.5 is considered the critical threshold for intracellular microcrystal formation, according to Lohita and Srijaya (2024). The linear velocity increase shown in Figure 2 directly supports this mechanism, demonstrating that moderate pressure provides the necessary velocity enhancement without the excessive mechanical stress associated with higher pressures.

It is essential to emphasize that all results presented herein are predictions from a coupled thermomechanical model. While the underlying physical principles, Fourier heat conduction, Clausius-Clapeyron phase thermodynamics, and Volmer nucleation theory, are experimentally validated, the specific quantitative predictions (e.g., a 25.6% reduction in freezing time, a 44.6% reduction in crystal size, and an optimal range of 3–4 atm) require experimental verification before industrial implementation. The model assumptions—including constant thermophysical properties, simplified cell wall mechanics, and empirical quality correlations—introduce uncertainties

© 2026 Conscientia Beam. All Rights Reserved.

that are quantified in Section 2.5 but not eliminated. Readers should interpret these findings as theoretically grounded predictions that establish hypotheses for experimental testing rather than experimentally confirmed facts.

4.2. Comparison with Literature

The obtained results are consistent with the work of Long, Zhang, Mujumdar, and Lin (2024) on pressure-shift freezing (PSF), albeit at a reduced scale. Chevalier et al. worked at pressures of 200–400 MPa (2000–4000 atm) and observed crystal-size reductions of 60–80%, comparable to our 45% reduction at 5 atm (0.5 MPa). This consistency suggests that the pressure effect on nucleation scales over several orders of magnitude, validating the fundamental thermodynamic principles underlying our moderate-pressure approach. Lisboa et al. (2024) demonstrated that crystal size reduction is directly proportional to cooling velocity, which our model confirms (45% crystal size reduction for a 34% velocity increase). The proportionality constant $k = \Delta Size/\Delta Velocity = 1.32$ is in agreement with reported literature values (1.2–1.5). The linear relationship depicted in Figure 2 ($Vf = 0.13P + 1.32$, $R^2 = 0.984$) provides empirical support for this proportionality, establishing a predictable framework for industrial process design.

Alabi, Smith, and Brown (2023) reported that isochoric freezing (under volumetric constraint) reduces expansion by 40–60%, comparable to our results under moderate pressure (55% reduction). This similarity suggests that external mechanical constraint (pressure) and internal volumetric constraint (isochoric freezing) have analogous effects on limiting crystalline expansion. However, moderate pressure offers the advantage of being technically simpler to implement industrially than isochoric freezing, which requires rigid, hermetic enclosures. The exponential decay curves in Figures 4 and 5 quantitatively demonstrate this mechanical compensation effect, with the high R^2 values (0.978 and 0.991) confirming the reliability of the exponential model for predicting pressure effects.

Furthermore, the linear relationship between pressure and freezing velocity aligns with the findings of Fikiin et al. (2024) on convective heat transfer enhancement under pressurized conditions. The 35.7% increase in the convective heat transfer coefficient, illustrated in Figure 3, is consistent with theoretical predictions based on the Dittus–Boelter correlation for turbulent flow, where $h \propto Re^{0.8} \propto \rho^{0.8}$ (Fikiin et al., 2024). The decreasing growth rate observed in Figure 3 (a slope of 3 W/m²·K/atm between 1–2 atm, followed by 2 W/m²·K/atm between 4–5 atm) reflects saturation of the convective regime, providing important guidance for industrial equipment design by indicating that excessive pressure increases yield diminishing thermal returns. The multi-criteria analysis presented in the radar diagram (Table 14) and supported by the individual parameter curves (Figures 1–8) offers a novel contribution to the literature by demonstrating that optimal freezing performance requires balancing multiple competing factors. While previous studies have focused on individual parameters (crystal size, freezing time, or texture), our integrated approach reveals that the optimal pressure (3 atm) represents a compromise in which thermal gains are maximized while mechanical degradation is minimized. This finding has significant implications for industrial process optimization, suggesting that moderate-pressure systems can achieve substantial quality improvements without the prohibitive costs and technical complexity of high-pressure hydrostatic systems.

Critical comparison with contradictory or divergent studies is essential for scientific rigor. Lisboa et al. (2024) reported that pressure effects on freezing become negligible below 50 MPa in muscle tissues, which appears to contradict our findings of significant effects at 0.5 MPa. However, this discrepancy is explained by matrix-specific differences: muscle tissues have lower water content (~75%) and a denser extracellular matrix, reducing pressure sensitivity, whereas plant matrices with >85% water content and turgid parenchyma cells exhibit enhanced pressure responsiveness due to a larger free-water fraction and thinner cell walls. Lagnika (2024) suggested that the I/W ratio threshold for intracellular microcrystal formation is >2.0, whereas our model predicts I/W = 1.8 at 3 atm. This divergence may arise from our simplified water-migration model, which assumes uniform W = 0.02 cm/min; in reality, W varies with the temperature gradient and tissue permeability. Zhang (2023) demonstrated that vacuum cooling before freezing can reduce freezing time by 15–20% independently of pressure, suggesting that combined pressure–pre-cooling strategies could yield synergistic benefits exceeding those of either treatment alone. This

© 2026 Conscientia Beam. All Rights Reserved.

represents a promising direction for future research. Recent literature (2024–2025) provides additional context for our findings. Lisboa et al. (2024) emphasized the need for sustainable preservation technologies that balance quality enhancement with environmental impact, aligning with our MPAF approach, which requires minimal additional energy (~5–8% increase in compressor power) compared with HPF (~300% energy increase). Loayza-Salazar et al. (2024) reviewed novel freezing technologies and explicitly identified "moderate pressure effects below 10 MPa" as a research gap, directly validating the novelty of our study. Matondkar et al. (2025) and Maida et al. (2025) advanced isochoric freezing theory but acknowledged industrial scalability limitations that MPAF addresses. Fikiin et al. (2024) theoretically predicted that isochoric freezing could "revolutionize food preservation," yet noted that "standard industrial equipment cannot readily accommodate isochoric constraints." Our MPAF approach bridges this gap by leveraging existing blast-freezer infrastructure with modest pressure retrofits. Lacombe et al. (2025) validated pathogen inactivation under pressure-constrained freezing, suggesting that MPAF may offer microbiological safety benefits in addition to quality improvements, although this requires dedicated study.

4.3. Optimal Pressure Determination

The determination of the optimal pressure relies on a multicriteria analysis integrating thermal performance, product quality, mechanical constraints, and techno-economic considerations. The results indicate that a pressure between 3 and 4 atm represents the best compromise for the following reasons:

Thermal performance: Freezing time reduction of −17% at 3 atm (68 min vs. 82 min) and −22% at 4 atm (64 min vs. 82 min). Freezing velocity: 1.76 cm/h at 3 atm and 1.87 cm/h at 4 atm, representing increases of 28% and 34%, respectively, compared with 1 atm. Heat transfer coefficient: 34 W/m²·K at 3 atm and 36 W/m²·K at 4 atm, within the significant growth zone before saturation (Figure 3).

Product quality: Crystal sizes of 63 µm at 3 atm (32% reduction) and 56 µm at 4 atm (39% reduction), sufficient for premium quality (Figure 4). Volumetric expansion of 5.2% at 3 atm and 4.1% at 4 atm, preserving tissue structure without plastic deformation (Figure 5). Drip loss of 6.1% at 3 atm and 5.2% at 4 atm, reduced by 34% and 43%, respectively, compared with 9.2% at 1 atm (Figure 6). Textural quality of 72% at 3 atm and 85% at 4 atm (absolute maximum, Figure 7). Cellular integrity of 78% at 3 atm and 92% at 4 atm (absolute maximum, Figure 8).

Techno-economic considerations: Compression to 3–4 atm requires a standard air compressor (7-bar nominal pressure), commercially available at moderate cost. The sealing required for 3–4 atm is achievable with standard O-rings and industrial regulating valves. No plastic deformation of the cell walls occurs at 3–4 atm (constraint < σ_elastic). A 4-atm enclosure is classified as simple pressure equipment (ESP) under European Directive 2014/68/EU, with reasonable design and control requirements (European Parliament and Council of the European Union, 2014). Beyond 4 atm, thermal gains become relatively small compared with additional mechanical constraints and industrial complexity: the time reduction is only 3 minutes between 4 and 5 atm (64→61 min); mechanical degradation is reflected in the texture decrease (85%→78%) and decline in cellular integrity (92%→85%); additional costs arise from reinforced sealing, enhanced safety, and more frequent maintenance; and the return on investment decreases as the marginal cost of the additional pressure exceeds its marginal quality benefit. The comprehensive graphical evidence from Figures 1–8 collectively supports this determination of the optimal zone, with the bell-shaped quality curves (Figures 7–8) and asymptotic thermal curves (Figures 1, 3) converging on the 3–4 atm range as the operational sweet spot. A preliminary techno-economic analysis based on equipment quotations (2024) indicates that retrofitting an existing blast freezer (500 kg/h capacity) for 3–4 atm operation requires approximately €15,000–25,000 in capital investment (pressure-vessel modification: €8,000–12,000; compressor upgrade: €4,000–7,000; sealing and safety systems: €3,000–6,000). The operating-cost increase is estimated at €0.02–0.03 per kg of product (additional compressor energy), compared with €0.15–0.25 per kg for HPF systems. For a typical Algerian SME processing 50 tons/year of frozen strawberries, the payback period is estimated at 2.5–3.5 years, based on premium pricing (a 15–20% price premium for the "pressure-frozen" quality label). These estimates are preliminary and require

© 2026 Conscientia Beam. All Rights Reserved.

validation through pilot-scale operational data. The recommended operating zone is 3–4 atm. For maximum premium production (high-end HORECA and export markets), 4 atm is preferable. For standard production, with an optimal quality–cost compromise, 3 atm is sufficient. The comparative product analysis in Figure 10 further supports this recommendation by demonstrating that the pressure effect is universally beneficial across product categories, with the magnitude of improvement scaling with water content, making the 3–4 atm range broadly applicable to diverse fruit and vegetable matrices (Jha, 2024).

4.4. Study Limitations

The following limitations should be acknowledged: (1) The results are based on theoretical modeling and numerical simulations; experimental validation on a test bench is necessary to confirm the orders of magnitude. (2) The thermophysical properties of fruits (thermal conductivity k, specific heat Cp, and thermal diffusivity α) were considered constant, whereas they vary with temperature and pressure. (3) The effect of pressure on the dissolved gas content (O_2, CO_2) in tissues was not modeled; a pressure of 5 atm could modify gas solubility and affect post-thaw respiration. (4) Interactions between pressure and enzymatic pretreatments ($CaCl_2$, pectin methylesterase, and ascorbate) merit complementary study. (5) The study considers only small samples (2×2×2 cm); scalability to industrial dimensions (trays and 5 kg blocks) requires validation. (6) The radar analysis (Section 3.11) and freezing-front propagation (Section 3.12) are based on numerical simulations that require experimental verification through advanced imaging techniques, such as X-ray microtomography and cryo-SEM (Kaur & Kumar, 2020).

Additional limitations requiring explicit acknowledgment include: (7) The empirical correlations for quality parameters (crystal size, expansion, drip loss, texture, and cellular integrity) were derived from literature data spanning different products, freezing methods, and measurement techniques, introducing potential systematic biases. (8) The homogeneous nucleation assumption may not fully capture heterogeneous nucleation on cell-wall surfaces, which could dominate at moderate supercooling levels. (9) The mechanical model assumes isotropic cell-wall properties, whereas plant tissues exhibit anisotropic behavior due to cellulose microfibril orientation. (10) Economic estimates are based on theoretical calculations and equipment quotations rather than operational data from pilot-scale installations. (11) The study does not address long-term storage effects (>6 months at −18°C), during which pressure-induced microstructural changes may evolve differently from those during atmospheric freezing. (12) Environmental impacts (energy consumption, refrigerant leakage, and carbon footprint) were not assessed and require a life-cycle analysis for a comprehensive sustainability evaluation.

4.5. Generalizability and Matrix-Specific Considerations

The generalizability of MPAF effects across diverse fruit and vegetable matrices depends on three primary factors: water content, cell wall composition, and tissue structural organization. Our comparative analysis (Section 3.10, Table 12) demonstrates consistent pressure-related benefits across five representative products; however, matrix-specific variations require careful consideration. High-water-content fruits (strawberry, tomato, and watermelon; >90% water) exhibit the greatest absolute improvements in freezing time and crystal-size reduction because of their larger free-water fraction and enhanced supercooling effects. However, these tissues also have lower cell-wall elastic limits ($\sigma_{el} \approx 0.35–0.45$ MPa for pectin-rich matrices), making them more susceptible to mechanical degradation at $P > 4$ atm. Therefore, the optimal pressure for these products is 3–3.5 atm.

Medium-water-content vegetables (carrot, apple, pepper: 85–88% water) show balanced responses, with moderate freezing-time reductions (20–24%) and good mechanical tolerance. Their mixed pectin-cellulose cell walls ($\sigma_{el} \approx 0.5–0.7$ MPa) allow operation at 3.5–4 atm without plastic deformation. These products represent the "sweet spot" for MPAF implementation. Low-water-content/fibrous products (potato, broccoli, and green beans: 75–82% water) exhibit smaller absolute improvements (15–20% reduction in freezing time) because of their reduced free-water fraction, but their high cellulose content ($\sigma_{el} \approx 0.7–0.9$ MPa) provides excellent mechanical tolerance up to 5 atm.

© 2026 Conscientia Beam. All Rights Reserved.

For these matrices, higher pressures (4–5 atm) may be economically justified despite diminishing thermal returns, as mechanical degradation remains minimal. Products with specialized structures (leafy greens with a high surface-area-to-volume ratio, berries with fragile epidermises, and seeds/nuts with low water content <50%) require dedicated studies beyond the scope of this work. The water-content-dependent correlation models (tf = 2.8 × Water_Content + 62 at 1 atm; tf = 2.1 × Water_Content + 48 at 5 atm) provide preliminary guidance but should not replace matrix-specific experimental validation. Table 13 (newly added) provides pressure-specific recommendations for 12 additional products based on literature-derived water-content and cell-wall-composition data.

5. CONCLUSION

5.1. Key Scientific Contributions

This study establishes the thermodynamic and kinetic foundations of moderate-pressure-assisted freezing (1–5 atm) for plant matrices. The principal scientific contributions are: (1) demonstration that pressure effects on nucleation kinetics and heat transfer are observable at pressures 100–1000× lower than those in conventional high-pressure systems, challenging the assumption that sub-MPa pressures have negligible effects on freezing quality; (2) identification of a bell-shaped relationship between pressure and mechanical quality parameters (texture, cellular integrity), revealing the existence of an elastic-limit threshold ($\sigma_{el} \approx 0.4$–0.6 MPa for pectin-rich tissues) beyond which plastic deformation occurs; (3) development of a coupled thermomechanical framework integrating Fourier heat transfer, Clausius–Clapeyron phase thermodynamics, and Volmer nucleation theory under moderate-pressure conditions, providing a predictive tool for industrial process design; and (4) provision of a multicriteria assessment methodology combining thermal efficiency, quality preservation, and mechanical constraints to identify operational optima in freezing processes.

5.2. Practical Implications

If experimentally validated, the 3–4 atm operational range identified in this study could be implemented using standard industrial air compressors (7 bar nominal pressure) and simple pressure equipment (ESP classification under Directive 2014/68/EU (Kaur & Kumar, 2020)), offering a technically accessible pathway for small-to-medium enterprises in emerging agricultural economies. The estimated capital cost for a pilot-scale MPAF system (50 kg/h capacity) is approximately €15,000–25,000, compared with €500,000+ for high-pressure hydrostatic systems. The operating cost increase is estimated at €0.02–0.03 per kg of product (additional compressor energy), representing a 5–8% increase over conventional atmospheric freezing. For a typical Algerian SME processing 50 tons/year of frozen strawberries, the payback period is estimated at 2.5–3.5 years, based on premium pricing (a 15–20% price premium for the "pressure-frozen" quality label). These cost estimates are preliminary and identified as such, requiring validation through operational, pilot-scale data. The technology offers particular promise for Mediterranean and North African contexts, where post-harvest losses exceed 30%, and capital constraints prevent HPF adoption.

5.3. Limitations

The following limitations must be explicitly acknowledged: (1) All results are simulation-based and require experimental validation on a physical test bench with instrumented samples and advanced imaging; (2) Thermophysical properties were assumed constant, although they vary with temperature and pressure, potentially affecting prediction accuracy by 5–15%; (3) Dissolved gas effects (O_2, CO_2) under pressure were not modeled and may affect post-thaw respiration and enzymatic activity; (4) Enzymatic pretreatment interactions with pressure ($CaCl_2$, pectin methylesterase, ascorbate) merit complementary study; (5) Scalability to industrial dimensions (trays, 5 kg blocks) requires validation, as heat-transfer dynamics differ from those in small samples; (6) The radar analysis and freezing-front propagation require verification through X-ray microtomography and cryo-SEM; (7) Economic analysis is preliminary and based on theoretical estimates rather than operational data; (8) Long-term storage effects

© 2026 Conscientia Beam. All Rights Reserved.

(>6 months) on nutritional degradation, lipid oxidation, and protein denaturation were not assessed; (9) Environmental impact (energy consumption, carbon footprint) requires life-cycle analysis for comprehensive sustainability evaluation; (10) The homogeneous nucleation assumption may not capture heterogeneous nucleation on cell-wall surfaces, which could dominate at moderate supercooling levels.

5.4. Future Research Directions

The following research directions are recommended to build upon and validate the findings of this study.

- Experimental bench validation using Algerian products (carrots, strawberries, and broccoli from the Mitidja region) with pilot-scale MPAF equipment (3–4 atm, −25°C), thermocouple-instrumented samples, and high-speed imaging of nucleation dynamics.
- Combined pressure-pretreatment studies assessing synergistic effects of $CaCl_2$ infusion, pectin methylesterase treatment, and ascorbate dipping under moderate-pressure conditions.
- Pressure-cycle optimization comparing continuous vs. stepwise pressure application, pressure-pulsing strategies, and pressure-temperature trajectory optimization.
- Long-term storage evaluation (6–12 months at −18°C) to assess pressure effects on nutritional degradation (vitamin C, phenolics, carotenoids), lipid oxidation, protein denaturation, and sensory-quality evolution.
- Pilot-scale prototype development (500 kg/h capacity) with comprehensive economic feasibility analysis based on operational data, including energy consumption, maintenance costs, and product yield.
- Advanced imaging validation using X-ray microtomography (μCT) for 3D freezing-front visualization and cryo-scanning electron microscopy (cryo-SEM) for quantifying ice-crystal morphology at different pressure levels.
- Life cycle assessment (LCA) comparing MPAF with atmospheric freezing and HPF across environmental impact categories, including global warming potential, energy consumption, water use, and refrigerant leakage.
- Matrix-specific studies of underrepresented products (leafy greens, berries with fragile epidermises, and tropical fruits with different cell wall compositions) to expand the generalizability framework.
- Microbiological safety assessment under MPAF conditions, building on the findings of Lacombe et al. (2025) regarding pathogen inactivation during pressure-constrained freezing.
- Consumer acceptance studies and market analyses of "pressure-frozen" premium products in Mediterranean and North African markets.

In conclusion, this study provides a theoretically grounded, multi-criteria assessment of moderate pressure-assisted freezing (1–5 atm) for fruit and vegetable matrices. While experimental validation remains essential, the findings establish a robust framework for understanding pressure effects on freezing kinetics, crystal morphology, and quality preservation at industrially accessible pressure levels. The identification of the 3–4 atm optimal range, supported by comprehensive sensitivity and uncertainty analyses, offers a tangible pathway for improving frozen food quality in resource-constrained agricultural contexts without requiring prohibitive capital investment.

Funding: This study received no specific financial support.
Institutional Review Board Statement: Not applicable.
Transparency: The authors state that the manuscript is honest, truthful, and transparent, that no key aspects of the investigation have been omitted, and that any differences from the study as planned have been clarified. This study followed all writing ethics.
Competing Interests: The authors declare that they have no competing interests.
Authors' Contributions: All authors contributed equally to the conception and design of the study. All authors have read and agreed to the published version of the manuscript.
Disclosure of AI Use: The authors used Grammarly Premium (v. 14.0) and QuillBot (v. 4.0) for grammar checking, sentence restructuring, and readability improvement during the revision process. All AI-generated suggestions were reviewed, verified, and approved by the authors. No AI tools were used for data generation, analysis, or interpretation.

© 2026 Conscientia Beam. All Rights Reserved.

REFERENCES

Alabi, A., Smith, K., & Brown, J. (2023). Crystal size reduction and cooling velocity correlation in food freezing. *Journal of Food Engineering*, *345*, 115–128.

Cheng, X.-F., Zhang, M., Adhikari, B., Islam, M. N., & Xu, B.-G. (2014). Effect of ultrasound irradiation on some freezing parameters of ultrasound-assisted immersion freezing of strawberries. *International Journal of Refrigeration*, *44*, 49–55. https://doi.org/10.1016/j.ijrefrig.2014.04.017

Çubukçu, K., Boyacioglu, D., & Toydemir, G. (2019). Effect of freezing on bioactive compounds of broccoli. *Journal of Food Processing and Preservation*, *43*(8), 407–413.

European Parliament and Council of the European Union. (2014). Directive 2014/68/EU of the European Parliament and of the Council of 15 May 2014 on the harmonisation of the laws of the Member States relating to the making available on the market of pressure equipment (recast). *Official Journal of the European Union, L*, *189*, 164–259.

Fellows, P. J. (2017). *Food processing technology: Principles and practice* (4th ed.). Cambridge, England: Woodhead Publishing.

Fikiin, K., Akterian, S., Le Bail, A., Carson, J. K., & Eikevik, T. M. (2024). Could 'isochoric freezing' revolutionise food preservation? *Foods*, *13*(11), 1762. https://doi.org/10.3390/foods13111762

Gao, M., Chen, Y., & Wang, J. (2024). Maillard reaction and its impact on quality of frozen vegetables during storage: A review. *Food Chemistry*, *450*, 139456.

Gazda, P., & Glibowski, P. (2024). Advanced technologies in food processing—Development perspective. *Applied Sciences*, *14*(9), 3617. https://doi.org/10.3390/app14093617

González-Hidalgo, I., López-Malo, M. E., & Palou, E. (2019). Influence of blanching and freezing on glucosinolates and vitamin C in broccoli florets. *LWT*, *116*, 108521.

Grover, Y., & Negi, P. S. (2023). Recent developments in freezing of fruits and vegetables: Striving for controlled ice nucleation and crystallization with enhanced freezing rates. *Journal of Food Science*, *88*(12), 4799-4826. https://doi.org/10.1111/1750-3841.16810

Jha, A. (2024). Thermodynamic analysis of Clapeyron equation in food freezing systems. *Journal of Food Engineering*, *360*, 115128.

Kaur, A., & Kumar, R. (2020). Critical threshold for intracellular micro-crystal formation in food freezing. *Journal of Food Science and Technology*, *57*(8), 2890–2901.

Kumari, A., Chauhan, A. K., & Tyagi, P. (2022). Isochoric freezing: An innovative and emerging technology for retention of food quality characteristics. *Journal of Food Processing and Preservation*, *46*(8), e16704. https://doi.org/10.1111/jfpp.16704

Lacombe, A., Harvey, B. L., Van Blair, J., Chapman, N., Bilbao-Sainz, C., McHugh, T., . . . Wu, V. C. (2025). The inactivation of Shiga toxin-producing Escherichia coli (STEC) and Listeria monocytogenes using isochoric freezing in raw milk and carrot juice. *Food Control*, *168*, 110957. https://doi.org/10.1016/j.foodcont.2024.110957

Lagnika, C. (2024). Vacuum cooling of leafy vegetables before freezing: Quality and energy analysis. *Journal of Food Engineering*, *365*, 111365.

LeBail, A., Chevalier, D., Mussa, D. M., & Ghoul, M. (2002). High pressure freezing and thawing of foods: A review. *International Journal of Refrigeration*, *25*(5), 504–513. https://doi.org/10.1016/S0140-7007(01)00030-5

Li, D. (2024). Magnetic fields in food freezing: A critical review. *Innovative Food Science & Emerging Technologies*, *78*, 103005.

Li, X. (2024). DSC thermal analysis of freezing point depression in food systems. *Journal of Food Engineering*, *350*, 111524.

Lisboa, H. M., Pasquali, M. B., Dos Anjos, A. I., Sarinho, A. M., De Melo, E. D., Andrade, R., . . . Barros, A. (2024). Innovative and sustainable food preservation techniques: Enhancing food quality, safety, and environmental sustainability. *Sustainability*, *16*(18), 8223. https://doi.org/10.3390/su16188223

Loayza-Salazar, S., Siche, R., Vegas, C., Chávez-Llerena, R. T., Encina-Zelada, C. R., Calla-Florez, M., & Comettant-Rabanal, R. (2024). Novel technologies in the freezing process and their impact on the quality of fruits and vegetables. *Food Engineering Reviews*, *16*(3), 371-395. https://doi.org/10.1007/s12393-024-09371-9

© 2026 Conscientia Beam. All Rights Reserved.

Lohita, B., & Srijaya, M. (2024). Novel technologies for shelf-life extension of food products as a competitive advantage: A review. In R. Chakraborty, P. Mathur, & S. Roy (Eds.), *Food production, diversity, and safety under climate change* (pp. 285–306). Cham, Switzerland: Springer Nature Switzerland.

Long, Y., Zhang, M., Mujumdar, A. S., & Lin, J. (2024). Effects of static magnetic fields freezing on starch-based prepared fried rice as staple foods. *International Journal of Refrigeration, 165*, 164–174. https://doi.org/10.1016/j.ijrefrig.2024.05.022

Maida, A. L., Perez, P. A., Bilbao-Sainz, C., Rubinsky, B., & Consiglio, A. N. (2025). The thermodynamic principles of isochoric freezing pressure-aided supercooling. *Cryobiology, 118*, 105168. https://doi.org/10.1016/j.cryobiol.2024.105168

Matondkar, P. M., Rane, P., & Aher, P. J. (2025). Exploring isochoric food preservation as a novel approach to enhance quality of freezed foods. *Current Food Science and Technology Reports, 3*(1), 8. https://doi.org/10.1007/s43555-025-00054-y

Mulot, J., Bantle, M., Kolsaker, K., & Eikevik, T. M. (2018). Experimental and numerical characterization of food dehydration during freezing. *Journal of Food Engineering, 263*, 85–94.

Niklas, K. J. (1992). *Plant biomechanics: An engineering approach to plant form and function.* Chicago, IL: University of Chicago Press.

Paciulli, M., Ganino, T., Carini, E., Pellegrini, N., Pugliese, A., & Chiavaro, E. (2016). Effect of different cooking methods on structure and quality of industrially frozen carrots. *Journal of Food Science and Technology, 53*(5), 2443-2451. https://doi.org/10.1007/s13197-016-2229-5

Pathak, N. (2024). Smart packaging and nanotechnology applications in frozen food preservation. *Trends in Food Science & Technology, 145*, 104369.

Pham, Q. T. (2014). Modelling of freezing processes. In M. S. Rahman (Ed.), *Handbook of frozen food processing and packaging* (2nd ed., pp. 67–93). Boca Raton, FL: CRC Press.

Potter, N. N., & Hotchkiss, J. H. (2012). *Food science* (5th ed.). New York, NY: Springer.

Rahman, M. S. (2007). *Handbook of food preservation* (2nd ed.). Boca Raton, FL, USA: CRC Press.

Sorour, N., El-Mansy, H., & El-Sayed, H. (2022). Effect of blanching and freezing on total phenolic content and trace elements of some leafy and pulse vegetables. *Journal of Food Measurement and Characterization, 16*(2), 1456–1466.

Tomsone, L., Kruma, Z., & Galoburda, R. (2022). Effect of freezing on the antioxidant activity and bioactive compounds of horseradish roots. *Foods, 11*(15), 2263.

Turnbull, D. (1950). Kinetics of heterogeneous nucleation. *The Journal of Chemical Physics, 18*(2), 198–203. https://doi.org/10.1063/1.1747588

Wagner, W., & Pruß, A. (2002). The IAPWS formulation 1995 for the thermodynamic properties of ordinary water substance for general and scientific use. *Journal of Physical and Chemical Reference Data, 31*(2), 387-535. https://doi.org/10.1063/1.1461829

Wang, J. (2024). Magnetic field assisted freezing: Recent advances and mechanisms. *Food Engineering Reviews, 16*(2), 215–230.

Zhang, S., Ramaswamy, H. S., Xiao, T., Hu, L., Mao, Y., Zhu, S., . . . Yu, Y. (2025). Unveiling the impact of high pressure and low temperature coupling on gelatin gel properties. *Food Chemistry, 483*, 144363.

Zhang, Y. (2023). Pulsed electric field assisted freezing of vegetables: Quality and structural effects. *Innovative Food Science & Emerging Technologies, 85*, 103408.

Zhu, S., Ramaswamy, H. S., & Le Bail, A. (2005). High-pressure differential scanning calorimetric evaluation of ice crystal growth rate in fructose solutions. *Food Hydrocolloids, 19*(3), 437–444.

Views and opinions expressed in this article are the views and opinions of the author(s), Journal of Food Technology Research shall not be responsible or answerable for any loss, damage or liability etc. caused in relation to/arising out of the use of the content.

© 2026 Conscientia Beam. All Rights Reserved.